First posted online on 7 November 2017 as 10.1242/dev.156323
Access the most recent version at http://dev.biologists.org/lookup/doi/10.1242/dev.156323

Knockout of the Arp2/3 complex in epidermis causes a psoriasis-like disease hallmarked by hyperactivation of transcription factor Nrf2

Rob van der Kammen [1], Ji-Ying Song [2], Iris de Rink [3], Hans Janssen [4], Stefania Madonna [5], Claudia Scarponi [5], Cristina Albanesi [5], Wim Brugman [3], Metello Innocenti [1,*]

[1] Division of Molecular Genetics, The Netherlands Cancer Institute, Plesmanlaan 121, Amsterdam, 1066 CX, The Netherlands

[2] Department of Experimental Animal Pathology, The Netherlands Cancer Institute, 1066 CX Amsterdam, The Netherlands

[3] Genomics Core Facility, The Netherlands Cancer Institute, 1066 CX Amsterdam, The Netherlands

[4] Division of Cell Biology II, The Netherlands Cancer Institute, Plesmanlaan 121, Amsterdam, 1066 CX, The Netherlands

[5] Laboratory of Experimental Immunology, Fondazione Luigi Maria Monti - Istituto Dermopatico dell'Immacolata (IDI) – IRCCS, 00167 Rome, Italy

* Author for correspondence (m.innocenti@nki.nl)

KEY WORDS: Arp2/3 complex, Nrf2, epidermis, psoriasis.

SUMMARY STATEMENT

Knockout of *arpc4* in mouse epidermis uncovers that the Arp2/3 complex controls keratinocytes' shape and transcriptome through an actin-based cell-autonomous mechanism that can influence epidermal morphogenesis and homeostasis.

ABSTRACT

Arp2/3 complex assembles branched actin filaments key to many cellular processes, but its organismal roles remain poorly understood. Here we employed conditional *arpc4* knockout mice to study the function of the Arp2/3 complex in the epidermis.

We found that depletion of the Arp2/3 complex by knockout of *arpc4* results in skin abnormalities at birth that evolve into a severe psoriasis-like disease hallmarked by hyperactivation of transcription factor Nrf2. Knockout of *arpc4* in cultured keratinocytes was sufficient to induce nuclear accumulation of Nrf2, upregulation of Nrf2-target genes and decreased filamentous actin levels. Furthermore, pharmacological inhibition of the Arp2/3 complex unmasked the role of branched actin filaments in Nrf2 regulation. Consistently, we unveiled that Nrf2 associates with the actin cytoskeleton in cells and binds to filamentous actin *in vitro*. Finally, we discovered that Arpc4 is downregulated in both human and mouse psoriatic epidermis. Thus, the Arp2/3 complex affects keratinocytes' shape and transcriptome through an actin-based cell-autonomous mechanism that influences epidermal morphogenesis and homeostasis.

INTRODUCTION

Actin-related protein (Arp2/3) complex consists of two Actin-related proteins (Arp2 and Arp3) and five additional Actin-related protein complex subunits (Arpc1-5) (Goley and Welch, 2006). The Arp2/3 complex catalyses the polymerization of monomeric actin (globular (G)-actin) into branched filaments (filamentous (F)-actin) thereby generating branched F-actin networks and mechanical forces in the cell (Goley and Welch, 2006; Rotty et al., 2013).

The genome of most eukaryotes contains a single gene encoding each Arp2/3-complex subunit (Goley and Welch, 2006). Mice and humans have instead two functional *arp3*, *arpc1* and *arpc5* loci, which give rise to paralogues with diverging sequences and slightly different functional properties (Abella et al., 2016). Biochemical reconstitution of the Arp2/3 complex revealed that Arpc2 and Arpc4 are critical for the structural integrity of the complex, whereas the other subunits have only variable effects on actin nucleation (Gournier et al., 2001). Accordingly, knockdown of either Arpc2 or Arpc4 leads to the downregulation of the Arp2/3 complex in a variety of cell types (Goley and Welch, 2006). For this reason, Arpc2 and Arpc4 are referred to as core subunits, whereas Arp2, Arp3, Arpc1, Arpc3 and Arpc5 are regarded as peripheral subunits.

The Arp2/3 complex regulates many actin-dependent processes, such as cell migration, endocytosis, vesicle trafficking, organelle remodelling, cell-cell and cell-matrix adhesion (Goley and Welch, 2006; Leyton-Puig et al., 2017; Rotty et al., 2013). In agreement with its central role in the cell, germ-line knockout of the Arp2/3 complex and that of its activators causes early embryonic lethality in most multicellular animal models (Stradal et al., 2004). Thus, whether and how the Arp2/3 complex affects developmental and homeostatic events remain two outstanding and largely unexplored issues. Although conditional knockout technologies can bypass embryonic lethality, targeting of the peripheral subunit Arpc3 has only produced an Arpc3-less Arp2/3 complex and minor alterations in the central nervous system (Kim et al., 2013b; Kim et al., 2015; Zuchero et al., 2015) and small intestine (Zhou et al., 2015). Surprisingly, the knockout of Arpc3 in the epidermis resulted in neonatal lethality and defective epidermal permeability barrier (EPB) despite a largely normal tissue architecture (Zhou et al., 2013).

Epidermis is a stratified self-renewing epithelium fulfilling essential protective functions (Simpson et al., 2011; Watt, 2014). The most abundant cells in the epidermis are keratinocytes that self-organize in tightly juxtaposed layers. Strong cell-cell adhesion and firm binding between keratinocytes and the underlying basement membrane confer the necessary robustness on to the epidermis (Simpson et al., 2011; Watt, 2014). The keratinocytes bound to the basement membrane form the basal layer that proliferates and can undergo either symmetric or asymmetric division, the former ensuring regenerative potential and the latter constant renewal of the epidermis (Sotiropoulou and Blanpain, 2012; Watt, 2014). The daughter cells positioned above the basal layer enter the spinous layer, where they exit the cell cycle and begin a complex differentiation process that reinforces intercellular junctions (Simpson et al., 2011). The upper granular layer consists of flattened keratinocytes characterized by a water-impermeable cornified envelope located beneath the plasma membrane. Finally, the outermost cornified layer contains dead squamous cells tightly linked together and devoid of internal organelles, which are constantly shed off (Segre, 2006). The keratinocyte differentiation program controlling epidermal morphogenesis and homeostasis involves profound signalling-regulated rearrangements of both the composition and the architecture of the (actin) cytoskeleton (Simpson et al., 2011).

A master regulator of epidermal homeostasis is Nuclear factor (erythroid-derived 2)-like 2 (NFE2L2 or Nrf2), a member of the cap-and-collar family of transcription factors (Sykiotis and Bohmann, 2010). Nrf2 binds to antioxidant response element located in the regulatory regions of its target genes, most of which promote detoxification from reactive oxygen species and toxic compounds (Gorrini et al., 2013; Sykiotis and Bohmann, 2010). Not surprisingly, compelling evidence associates deregulation of Nrf2 expression and/or activity to a number of pathologies (Schafer and Werner, 2015; Sykiotis and Bohmann, 2010). In homeostasis, the levels of Nrf2 are controlled by a Keap1-containing Cullin 3-based E3 ligase complex that binds and ubiquitinates Nrf2 in the cytosol thereby dooming it for proteasome-mediated degradation (Sykiotis and Bohmann, 2010). In stressed cells, Keap1 no longer ubiquitinates Nrf2, which can accumulate and translocate into the nucleus where it promotes gene transcription (Sykiotis and Bohmann, 2010).

Here, we report that ablation of the Arp2/3 complex in mouse epidermis causes a severe psoriasis-like disease hallmarked by Nrf2 hyperactivation and decreased F-actin levels. Unexpectedly, we find that the Arp2/3 complex modulates Nrf2-dependent gene transcription in keratinocytes by regulating Nrf2 localization through a mechanism that involves binding of Nrf2 to actin filaments. The finding that the Arp2/3 complex couples actin-based regulation of keratinocytes' shape and transcriptome, which can influence epidermal morphogenesis and homeostasis, opens a new view on its mode of action. Furthermore, the downregulation of Arpc4 in both human and mouse psoriatic epidermis suggests a possible role for the Arp2/3 complex in psoriasis pathogenesis.

RESULTS

Knockout of *arpc4* in mouse epidermis results in Arp2/3-complex null keratinocytes

We exploited a mutant (flox = *f*) allele of the Arp2/3-complex core subunit *arpc4* (Fig. 1A) to obtain homozygous *arpc4*$^{f/f}$ mice on a pure B6 genetic background (Fig. 1B). As homozygous germ-line deletion of *arpc4* was embryonic lethal *prior* to E7.5 (not shown), transgenic *arpc4*$^{f/wt}$ mice expressing Cre recombinase downstream of Keratin 14 promoter were crossed with the *arpc4*$^{f/f}$ mice to ablate the expression of Arpc4 in the hair follicles and basal cells of the epidermis (Fig. 1C). The resulting offspring was composed by all four genotypes in an expected mendelian ratio, including epidermis-specific *arpc4* KO (hereafter referred to as *arpc4* eKO) mice (Fig. 1C). The *arpc4* eKO pups could be easily recognized from the macroscopic appearance of the skin, which displayed uneven thickening accompanied by alopecic areas (Fig. 1D, Movie 1). The expression of Arpc4 and Arpc1A were dramatically decreased in these epidermal regions (Fig. S1A). Keratinocytes isolated from the abnormal areas of the *arpc4* eKO pups were not only devoid of Arpc4 but also lacked the entire Arp2/3 complex (Fig. S1D), thus confirming that the core subunits are essential for the stability of the Arp2/3 complex.

Knockout of *arpc4* in mouse epidermis causes a psoriasis-like disease

Initial skin lesions were detected microscopically in the *arpc4* eKO mice at day 1 after birth (post-natal (PN) day 1). Local thickening of the epidermis, mainly the cornified layer, and the presence of scattered "ghost cells" (anucleated cells) were particularly obvious in the head region (Fig. 1E). These initial lesions developed progressively into macroscopic psoriasis-like plaques: body and extremities of the *arpc4* eKO mice had a dry, unevenly thickened and poorly furred skin at PN5 (Fig. 1D). Furthermore, microscopic analyses revealed abnormal thickening of the cornified layer (hyperkeratosis), presence of nuclei in the cornified layer (parakeratosis) accompanied by microabscesses, and hyperplasia of the epidermal squamous cells (acanthosis) at day 7 after birth (Fig. 1E). In addition, hair follicles in the psoriasis-like lesions were rare and often lacked the shaft and the sebaceous gland (Fig. 1E, Fig. S1C). Inflammatory infiltrations mainly consisting of lymphocytic cells were observed in dermis (dermatitis) (Figs 1E, Fig. S1C, inset i and iii). The psoriasis-like lesions progressed further over time and acquired an ichthyosis-like appearance (Fig. 1E). Ultrastructural analyses confirmed the above observations and further showed that the *arpc4* eKO mice have no evident signs of compromised epidermal integrity (Fig. 1F). Consistently, the *arpc4* eKO pups mounted a fully functional outside-in EPB (Fig. S1D) and EPB regulators YAP/TAZ (Zhou et al., 2013) attained normal activity both *in vivo* and in isolated keratinocytes (Fig. S2A,B). Inside-out EPB could not be reliably probed because epidermal lesions are microscopic in *arpc4* eKO newborns. Thus, we cannot exclude a mild inside-out EPB defect. In any case, the *arpc4* eKO animals had to be euthanized by post-natal day 21 due to the severity of the skin lesions.

Molecular characterization of the *arpc4* eKO skin with well-established differentiation markers (cornified envelope regulator Transglutaminase 1 (Matsuki et al., 1998), cornified envelope component Involucrin (Koch et al., 2000), suprabasal Keratin 1 (Roth et al., 2012) and basal and stem-cell Keratin 15 (Bose et al., 2013)) showed that ablation of Arp2/3 complex perturbs the differentiation program of keratinocytes (Fig. S1E). In addition, skin lesions showed increased Ki67 positivity in both the basal and the suprabasal epidermal layers (not shown).

Although the psoriasis-like lesions were of variable size and usually more severe in the dorsal than in the ventral trunk, extremities and head (Movie S1), the disease showed full penetrance. The patchy nature of the phenotype was somewhat surprising as K14-Cre-mediated recombination gives a mosaic pattern at day E15 and occurs in most of the epidermis after birth (Huelsken et al., 2001). However, flox alleles that remain largely mosaic after birth have been previously reported (Kobielak et al., 2003; Raymond et al., 2005). Since lesions were located in the areas of the epidermis with no Arp2/3 complex expression and the *arpc4* eHet mice were normal (Fig. S1A and not shown, respectively), mosaic recombination of the *arpc4* flox allele likely explains the above findings. Overall, these observations indicate that ablation of the Arp2/3 complex in the mouse epidermis perturbs epidermal cell differentiation and causes a psoriasis-like disease.

arpc4 eKO epidermis displays a psoriasis-like gene expression profile

To characterize this phenotype at the molecular level, we determined the global gene expression profile of the epidermis of wild-type and *arpc4* eKO siblings. Comparative analysis of RNA sequencing (RNA-seq) data identified 141 differentially expressed transcripts, most of which (131) were upregulated upon knockout of *arpc4* (Fig. 2A, Table S1). RT-qPCR analysis of independent epidermal samples supported the validity of this gene signature (Fig. 2B). Ingenuity Pathway Analysis (IPA) allowed us to extract system-level patho-physiological information from the list of *arpc4*-responsive genes. The category "Dermatological Diseases and Conditions" ranked first among the IPA-annotated diseases and disorders and most of the other top categories were related to events often observed in psoriasis, such as inflammatory response (Fig. 2C, Table S2). In agreement with the anatomo-pathological analysis of the skin of the *arpc4* eKO mice, psoriasis was the most enriched "disease or functions annotation" belonging to the "Dermatological Diseases and Conditions" (Fig. 2D, Table S2). In summary, the gene expression profiles of the epidermis of the wild-type and the *arpc4* eKO mice confirm the diagnosis based on anatomo-pathological criteria.

Transcription factor Nrf2 is hyperactive in the epidermis of *arpc4* eKO mice

The RNA-seq data revealed an unexpected connection between the function of the Arp2/3 complex and that of Nrf2: among the genes showing a significantly altered expression in wild-type *vs. arpc4* eKO mice, 65 were Nrf2-responsive genes (Table S1). Instead, only one target (*parp8*) of G-actin-sensitive myocardin-related transcription factor (MRTF) (Esnault et al., 2014; Posern and Treisman, 2006) was significantly affected. Thus, the G-actin pool controlling MRTF activity is apparently independent of the Arp2/3 complex.

Remarkably, mice with enhanced Nrf2 activity in keratinocytes present severe hyperkeratosis and acanthosis of the epidermis (Schafer et al., 2012) resembling the initial abnormalities observed in the *arpc4* eKO mice. This and the observation that most differentially expressed genes are upregulated upon knockout of *arpc4* suggest that the Arp2/3 complex may restrain Nrf2 activity in keratinocytes. Consistent with this hypothesis, the epidermis of the *arpc4* eKO mice showed increased nuclear Nrf2 levels at day 4 (Fig. 3A). The number of Nrf2-positive interfollicular keratinocytes declined with age in the normal epidermis, but Nrf2 expression remained ubiquitous in the psoriasis-like lesions (Fig. 3B). Of note, neither the mRNA (852 -/+ 68 (n = 3) and 686-/+ 52 (n = 3) reads in wild-type and eKO epidermises, respectively; $p = 0.12$, unpaired two-tail T-test) nor the protein levels of Keap1 were downregulated in the *arpc4* eKO mice (Fig. 3B). This rules out that the Arp2/3 complex inhibits Nrf2 by controlling Keap1 expression. Most importantly, Nrf2-target genes identified by RNA-seq (Sprr2, Keratin 6 (Krt6) and S100a9), as well as genuine Nrf2-target gene NQO1, attained increased protein levels in the affected epidermal areas (Fig. 3B). Thus, Nrf2 is hyperactive in the epidermal regions devoid of the Arp2/3 complex.

The Arp2/3 complex regulates Nrf2 localization and activity in keratinocytes

To prove that ablation of *arpc4* in basal keratinocytes increases Nrf2 activity, we isolated wild-type and *arpc4* KO keratinocytes. As expected, the knockout cells lacked both lamellipodia and ruffles and showed a global reduction in the F-actin levels, stress fibers included (Fig. S3A). Of note, reduced F-actin levels could also be observed in the psoriatic epidermis of the *arpc4* eKO mice (Fig. S3B). Phosphorylated Nrf2 levels were higher in the *arpc4* KO than the wild-type keratinocytes (Fig. 4A), suggestive of increased Nrf2 activity. Compared with wild-

type keratinocytes, the *arpc4* KO keratinocytes and those overexpressing Nrf2 (see also Fig. 7A) displayed a very similar, mainly upregulated, gene expression pattern (Fig. 4B,C, Table S3). Furthermore, silencing of Nrf2 in the *arpc4* KO keratinocytes attenuated the expression of Nrf2-responsive genes identified by RNAseq (Fig. 4D,E), but did not rescue the actin cytoskeleton (Fig. S3C). Collectively, these results show that the Arp2/3 complex regulates Nrf2 activity in keratinocytes.

To elucidate the underlying molecular mechanism, we expressed EGFP-tagged Arpc4 and empty EGFP in two independent populations of *arpc4* KO keratinocytes to generate rescued and knockout isogenic lines, respectively (Fig. 5A). Molecular characterization of these keratinocytes indicated that the introduction of EGFP-Arpc4 in the *arpc4* KO cells was sufficient to rescue the endogenous Arp2/3-complex subunits, whereas it did not affect either Nrf2 or Keap1 expression (Fig. 5A). Morphological characterization of the isogenic EGFP- and EGFP-Arpc4-expressing *arpc4* KO keratinocytes showed that the former are smaller, have reduced F-actin levels and lack lamellipodia, whereas they often display bleb-like structures and fewer stress fibers (Fig. 5B, Fig. S4A). This latter observation is in line with the filaments assembled by the Arp2/3 complex being incorporated into stress fibers (Hotulainen and Lappalainen, 2006). Fractionation experiments confirmed biochemically that F-actin is decreased in the absence of the Arp2/3 complex (Fig. 5C,D, Fig. S4B). Consistent with the well-established localization of the Arp2/3 complex (Rotty et al., 2013), EGFP-Arpc4 decorated actin-rich lamellipodia and dotty cytoplasmic structures likely corresponding to vesicles and vesicular compartments (Fig. 5B, Fig. S4A).

The knockout keratinocytes showed more than a two-fold increase in the nuclear *vs.* cytosolic Nrf2 ratio compared with that of the rescued ones (Fig. 6A,B), which correlated with a higher expression of a battery of genuine Nrf2-responsive genes, including direct target *sprr2*, *sprr1* and *epgn* (Papp et al., 2012; Schafer et al., 2012; Schafer et al., 2014) (Fig. 6C). Therefore, regulation of Nrf2 localization and activity by the Arp2/3 complex is cell-autonomous in keratinocytes.

Actin nucleation by the Arp2/3 complex controls Nrf2 localization and activity

We failed to show that the Arp2/3 complex interacts with Nrf2 (not shown), but found that phosphorylation of Nrf2 at Ser40 increases in keratinocytes treated with Arp2/3 complex inhibitor CK-666 (Nolen et al., 2009) (Fig. 7A). Notably, phosphorylation of

Ser40 promotes nuclear accumulation and activation of Nrf2 (Huang et al., 2002). Consequently, we hypothesized that the Arp2/3 complex could control Nrf2 through the polymerization of actin filaments and explored this possibility further. As five different commercial anti-Nrf2 antibodies cross-react with additional proteins in keratinocytes, we carried out single-cell analyses exploiting a keratinocyte line expressing EGFP-tagged Nrf2 at low levels (Fig. 7B, Fig. S5A). Upon CK-666 treatment, the number of cells having a higher EGFP-Nrf2 signal in the nucleus than in the cytosol doubled (Fig. 7C,D). The observed cell-to-cell variability is most likely inherent to the polyclonal nature of keratinocytes. Live-cell imaging confirmed that pharmacological inhibition of the Arp2/3 complex leads to nuclear accumulation of EGFP-Nrf2 (Fig. S5B, Movie S2). Alike CK-666, actin depolymerisation induced by Latrunculin A caused the nuclear accumulation of EGFP-Nrf2 in keratinocytes (Fig. 7E,F). Instead, inhibition of formin-induced actin polymerization by SMIFH2 (Isogai et al., 2015b) had no significant effects (Fig. 7E,F). The sum of these results points towards a specific role for the actin filaments nucleated by the Arp2/3 complex in the control of Nrf2 localization.

In agreement with the above results, CK-666 treatment also stimulated the expression of Nrf2-target genes in both wild-type and EGFP-Nrf2-expressing keratinocytes (Fig. S5C). This functionally links Arp2/3-complex-mediated actin polymerization and Nrf2 activity and also support the physiological relevance of this new Nrf2-regulatory mechanism.

Surprisingly, EGFP-Nrf2 partially co-localized with F-actin in lamellipodia and along stress fibres (Fig. 7G). This localization pattern was clearly perturbed by CK-666 and Latrunculin A, but not SMIFH2 (Fig. S6). Thus, the presence of Nrf2 on F-actin structures seems to be largely dependent on the actin nucleation activity of the Arp2/3 complex. Co-sedimentation assays showed that purified full-length GST-Nrf2 (Fig. 8A) binds directly to F-actin at concentrations that mimic the low steady-state levels of Nrf2 in the cell (Kim et al., 2011) (Fig. 8B). Congruently, the equilibrium dissociation constant of the Nrf2-F-actin interaction lies in the high nanomolar range (Fig. 8C). *In vivo*, however, only the actin filaments nucleated by the Arp2/3 complex are permissive for the binding of Nrf2. Noteworthy, the initial branched geometry of these filaments excludes actin-binding proteins that decorate linear actin networks (Michelot and Drubin, 2011) and may outcompete Nrf2.

In summary, binding of Nrf2 to F-actin unveils that Nrf2 regulation by the Arp2/3 complex involves actin nucleation.

Arpc4 expression is downregulated in both human and mouse psoriatic skin

The phenotype of the *arpc4* eKO mice suggests that the Arp2/3 complex may be involved in the pathogenesis of psoriasis. However, population-based studies in humans have not yet revealed an association between *arpc4* and psoriasis. Hence, we first analysed Arpc4 expression and distribution in the skin of healthy donors by immunohistochemistry. Human epidermis showed a rather uniform positivity for Arpc4 both in the basal and supra-basal layers (Fig. 9A, Fig. S7). This expression pattern strongly resembles that of mouse Arpc4 (Fig. S1A). Notably, Arpc4 was particularly abundant within the nucleus in roughly half of the analysed healthy skin samples, as well as in uninvolved psoriatic skin (Fig. S7). This suggests that nuclear Arpc4 is not predisposing to or protecting from psoriasis. Next, healthy skin was compared to both uninvolved and lesional skin of psoriatic patients. We found that Arpc4 expression and distribution are similar in the epidermis of uninvolved skin of psoriatic patients and healthy donors (Fig. 9A,B, Fig. S7). Nevertheless, reduced basal Arpc4 levels were observed in two uninvolved psoriatic skin samples (Fig. S7), thus raising the possibility that dowregulation of the Arp2/3 complex is pathogenic in human epidermis. More importantly, Arpc4 immunoreactivity was significantly decreased in the epidermis of lesional psoriatic skin, especially in the basal proliferative layer (Fig. 9A,B, Fig. S7).

To corroborate the link between reduced Arpc4 expression and psoriasis, we used the imiquimod (IMQ)-induced psoriasiform mice model, which closely resembles the human psoriatic lesions in terms of phenotypic and histological characteristics, including epidermal hyperplasia (acanthosis) and the presence of inflammatory infiltrates in the dermis (van der Fits et al., 2009). As expected, B6 mice treated with IMQ showed *i)* a remarkably increased epidermal thickness (198.45 -/+ 48.03 μm and 40.06 -/+ 13.04 μm in IMQ-treated and control mice, respectively, $p < 0.001$), *ii)* thickening of the cornified layer (71.85 -/+ 34.56 μm vs. 29.22 -/+ 17.09 μm, $p < 0.001$), *iii)* perturbed Krt10 expression indicative of impaired terminal differentiation (Fig. 9C), *iv)* enhanced proliferation hallmarked by a Ki67-positive keratinocytes (Fig. 9C), and *v)* widespread inflammatory infiltrate (not shown), when compared to

the control ones. In addition to these psoriasis-like manifestations, Arpc4 expression was diminished in the IMQ-treated epidermis, especially that localized in the basal layer keratinocytes (Fig. 9C).

Therefore, the association between low Arpc4 expression and psoriasis appears to be conserved in mice and humans.

DISCUSSION

Here we report that the *arpc4* epidermal knockout mice are Arp2/3-complex null and develop severe psoriasis-like lesions hallmarked by ubiquitous Nrf2 expression and upregulation of Nrf2-target genes. Furthermore, we discovered that the Arp2/3 complex inhibits Nrf2 activity through a cell-autonomous mechanism involving the interaction between Nrf2 and F-actin. The downregulation of Arpc4 in human and mouse psoriatic skin suggests that the function of the Arp2/3 complex in the epidermis is conserved. Most importantly, our findings ascribe an unforeseen gene transcription-regulatory role to the actin network generated by the Arp2/3 complex in health and disease.

We propose a sequestration model to explain how the Arp2/3 complex harnesses the activity of Nrf2 in keratinocytes: actin nucleation by the Arp2/3 complex results in the formation of branched actin filaments that can be subsequently remodelled and incorporated into linear actin structures. The filaments generated by the Arp2/3 complex sequester part of the cytosolic Nrf2 pool and restrain the activity of Nrf2. Genetic ablation and pharmacological inhibition of the Arp2/3 complex relieve Nrf2, which can translocate into the nucleus where it increases the transcription of genes involved the psoriatic response. Notably, we provide robust experimental evidence in support of the tenets of this model.

First, the marked reduction in F-actin observed in the *arpc4* eKO mice (Fig. S2B) shows that the Arp2/3 complex is active in the “unchallenged” epidermis and can effectively participate in Nrf2 regulation. Thus, this new actin-based Nrf2-regulatory mechanism may functionally connect the reduction in F-actin levels with the rise in Nrf2 activity during keratinocyte differentiation (Schafer and Werner, 2015; Vaezi et al., 2002). It also suggests that the knockout of *arpc3* does not phenocopy that of *arpc4* because Arpc3-less Arp2/3 complex ensures normal epidermal F-actin levels (Zhou et al., 2013). Instead, the EPB defect and the perinatal lethality observed in the

arpc3 eKO mice likely stem from spurious dominant effects exerted by mislocalized Arpc3-less Arp2/3 complex on tight junctions and YAP/TAZ (Zhou et al., 2013).

Second, genetics and chemical biology show that the Arp2/3 complex assembles actin filaments endowed with unique Nrf2-regulatory features. The knockout of *arpc4* revealed that the Arp2/3 complex regulates both the branched and the linear F-actin networks (Fig. 5B, Fig. S3A) to which Nrf2 can associate (Fig. 7G, Fig. 8, Fig. S6). Nevertheless, mice lacking either FMN1 or mDia1, formins that polymerize linear actin filaments in epithelial cells (Isogai et al., 2015d; Kobielak et al., 2004), do not have skin defects (Eisenmann et al., 2007; Wynshaw-Boris et al., 1997). Furthermore, pan-formin inhibitor SMIFH2 failed to affect the localization of EGFP-Nrf2 (Fig. 7E,F, Fig. S6), the phosphorylation of Nrf2 at Ser40 (Fig. 7A) and the expression of Nrf2-target genes in keratinocytes (not shown). Hence, remodelling of Nrf2-bound branched actin filaments likely explains the localization of Nrf2 on linear F-actin structures. Most importantly, these observations show that the initial branched geometry of the actin filaments nucleated by the Arp2/3 complex is a key Nrf2-regulatory feature. Remarkably, we also discovered that the Arp2/3 complex restrains Nrf2 phosphorylation on Ser40 (Fig. 4A, Fig. 7A), which favours nuclear accumulation and activation of Nrf2 (Huang et al., 2002). Hence, Nrf2 regulation by the Arp2/3 complex involves both binding to F-actin and a post-translational modification. In this regard, it has been proposed that Keap1 forms a complex with F-actin and Nrf2 thereby promoting ubiquitination and proteasome-mediated degradation of Nrf2 in the cytosol (Kang et al., 2004). However, this is highly unlikely because the same region of Keap1 interacts with actin and Nrf2 (Kang et al., 2004) and cellular actin is so abundant to fully outcompete Nrf2. Not surprisingly, subsequent studies have excluded that the actin cytoskeleton allows Keap1 to control Nrf2 (Velichkova and Hasson, 2005). In any case, we found that Keap1 is diffused and uniformly distributed in keratinocytes expressing EGFP-Nrf2 (Fig. S8). This latter observation is consistent with the cell type-specific localization of Keap1 at actin-positive structures (Velichkova et al., 2002). Therefore, the Arp2/3 complex and Keap1 regulate Nrf2 through entirely distinct mechanisms. As neither Nrf2 nor Keap1 levels vary upon knockout of *arpc4* in keratinocytes (Fig. 5), it also appears that the Arp2/3 complex and Keap1 act independently on Nrf2.

Third, the knockout of *arpc4* resulted in decreased F-actin levels both *in vivo* and in isolated keratinocytes (Fig. S3B, Fig. 5D). Although this involved both branched and linear F-actin structures (Fig. 5B, Fig. S3A), the knockout of *arpc4* had negligible effects on the expression of MRTF-target genes (Fig. 2A, Fig. 4B). Intriguingly, we also found that the expression of Nrf2-target genes is insensitive to formin inhibition (not shown). Therefore, keratinocytes have distinct F-actin and G-actin pools regulated by either the Arp2/3 complex or formins, as well as independent mechanisms to sense and respond to the changes in either F-actin network.

Fourth, knockout of *arpc4* in basal keratinocytes causes a psoriasis-like disease hallmarked by Nrf2 hyperactivation (Fig. 1, Fig. 2, Fig. S1) and downregulation of Arpc4 occurs in both human psoriatic skin and the IMQ-induced psoriasis mouse model (Fig. 9). Moreover, elevated expression of Nrf2 has been recently observed in psoriasis and suggested to cause pathogenic hyperproliferation of keratinocytes (Yang et al., 2017). Hence, the phenotype of the *arpc4* eKO mice may be partly due to Nrf2 hyperactivation enhancing keratinocyte proliferation *in vivo*. The similarities between the early phenotype of the *arpc4* eKO mice and that of mice expressing constitutively active Nrf2 in basal keratinocytes support this view (Schafer et al., 2012). As only the knockout of *arpc4* causes a psoriasis-like disease in mice, Nrf2-independent regulation of gene transcription and actin dynamics by the Arp2/3 complex also has a key physiopathological role. The use of Nrf2 activator Dimethyl Fumarate (DMF) to treat moderate-to-severe plaque psoriasis does not contradict the pathogenic role of Nrf2 in psoriasis. Actually, the anti-inflammatory and immune-modulatory properties of DMF may not require Nrf2 (Schulze-Topphoff et al., 2016) and could counteract cell proliferation driven by the further activation of Nrf2 in psoriatic skin. Alternatively, the beneficial anti-inflammatory and cytoprotective functions of Nrf2 may prevail over its pathogenic proliferative role in the epidermis only above a certain expression level and/or in full-blown psoriatic lesions.

In any case, downregulation of the Arp2/3 complex in keratinocytes qualifies it as one of the elusive epidermal cell-intrinsic psoriasis triggers. In line with this idea, the psoriasis-like disease in the *arpc4* eKO mice is not due to a generic pro-inflammatory response in keratinocytes. In fact, *arpc4* ablation did not increase the levels of active, phosphorylated NF-κB in isolated keratinocytes (Fig. 4A) nor did it produce

upregulation and enrichment of NF-κB-target genes in the epidermis (Fig. 2A). Similarly, we also ruled out early disruption of the basement membrane in the *arpc4* eKO pups as the primary cause of the psoriasis-like disease (Fig. S9). Given that the Arp2/3 complex is essential for embryogenesis, we propose that epigenetic events and/or somatic mutations determine Arp2/3-complex levels in the epidermis. Arpc4 downregulation by IMQ in mouse epidermis (Fig. 9C) supports this view.

In summary, we have discovered that the Arp2/3 complex affects epidermal morphogenesis and homeostasis by coupling actin-based regulation of keratinocytes' shape and transcriptome. These unforeseen findings pave the way for a deeper understanding of the cellular and organismal functions of the Arp2/3 complex in health and disease.

MATERIALS AND METHODS

Mice

Arpc4$^{tm1a(EUCOMM)Wtsi}$ mice (knockout-first mice with conditional potential, promoterless cassette) were obtained from the Wellcome Trust Sanger Institute. These mice were backcrossed with Flp recombinase transgenic C57Bl/6NRj mice to remove the cassette flanked by Frt sites thereby creating conditional *arpc4*$^{wt/f}$ mice. *arpc4*$^{wt/f}$ mice were backcrossed on a C57Bl/6 background at least 10 times, before intercrossing *arpc4*$^{wt/f}$ mice to obtain homozygous *arpc4*$^{f/f}$ animals. *arpc4*$^{f/f}$ mice were phenotypically identical to wild-type B6 mice and bred well. Heterozygote K14-Cre(neo) transgenic B6 mice (Margadant et al., 2009) were backcrossed at least 10 time with C57Bl/6 mice before breeding with homozygous *arpc4*$^{f/f}$ mice. Analysed mouse cohorts consisted of both sexes. Genotyping of the *arpc4* alleles was done with the wild-type primers (Arpc4_39529_F: AAGCCTTGCCCGAGATAATG; Arpc4_39529_R: AAGCAAAGCCAGTCCCTCAC), whose position schematically depicted in Fig. 1A.

IMQ-induced mouse model of human psoriasis

Eight-week-old female C57BL/6 mice (Harlan Laboratories, San Pietro al Natisone, Italy) were divided randomly into control (n = 6) and IMQ-treated (n = 12) groups. While control mice received a control cream (Vaseline; Walgreens Pharmacy), IMQ-

treated mice received on the shaved back skin a daily topical dose of 50 mg of 5% IMQ cream (Aldara, Meda AB, Solna, Sweden). On day 5, skin biopsies of the treated area were collected with a 8-mm biopsy puncher, as previously described (Palombo et al., 2016). Epidermal and scale thickness, and cell infiltrate number were analyzed as parameters of skin acanthosis and inflammation (not shown). The significance of differences between experimental groups (mice treated with control cream *vs*. mice treated with IMQ) was calculated by unpaired Student's t-test (p values < 0.05 were considered significant).

Generation and culturing of keratinocytes

Keratinocytes were isolated from back skin epidermis of *arpc4*$^{f/f}$ and *arpc4*$^{f/f}$*::K14*-Cre(neo) littermates up to PN4. In brief, skins were removed, put on sterile 3MM paper and trypsinized (EDTA-free 0.25% trypsin) for 16 h at 4°C to separate the epidermis from the dermis. Epidermises were minced, and cells were detached by stirring on ice for 1 h. Cell suspensions were filtered and seeded on dishes coated with 10 µg cm^{-2} collagen IV (Becton Dickinson) and cultured in Epilife with 40 µM $CaCl_2$ and EpiLife-defined growth supplement (EDGS).

Primary keratinocytes grown in EpiLife medium containing 40 mM $CaCl_2$ and EDGS were immortalized with SV40 large T antigen as previously described (Mertens et al., 2005). Immortalized *arpc4*$^{f/f}$ keratinocyte cultures subsequently were treated with Adeno-cre virus produced in HEK293A cells to knock out *arpc4*. Rescue of the *arpc4*$^{f/f}$*::K14*-Cre(neo) (line #1) and *arpc4*$^{-/-}$ (line #2) populations devoid of Arpc4 was performed by retroviral transduction with pMX encoding either EGFP or human Arpc4 tagged with EGFP at the C-terminus. After 2-3 rounds of transduction, EGFP-positive keratinocytes were sorted. EGFP-Nrf2-expressing keratinocytes were generated from an immortalized *arpc4*$^{f/f}$ keratinocyte line by retroviral transduction with pMX encoding human Arpc4 tagged with EGFP at the N-terminus. Low passage (< 18) keratinocytes were used for experiments.

Nrf2 KD keratinocytes were obtained by transducing *arpc4* KO cells with lentiviruses encoding shRNA TRCN0000012129 (#1) and shRNA TRCN0000054658 (#2) targeting mouse NFe2L2. Control KD *arpc4* KO keratinocytes were obtained by transduction with empty pLKO-derived lentiviral particles prepared as previously described (Leyton-Puig et al., 2017). Low passage (< 18) keratinocytes were used for experiments.

Keratinocytes were divided using TrypLE Express enzyme (Invitrogen) and trypsin inhibitor (1 mg ml^{-1} (Sigma)) and plated in CELLnTEC Keratinocyte medium on collagen I-coated dishes. After 24 hours, EpiLife medium containing 40 mM $CaCl_2$ and EDGS supplement was added. Only mycoplasma-free cells were used in all experiments.

(Immuno)histochemistry

Back skins (or decapitated bodies, PN1) were fixed in EAF (4% Formaldehyde, 5% Glacial acetic acid) and embedded in paraffin. Sections (5 μm) were deparaffinised and rehydrated, subjected to antigen retrieval and inactivation of endogenous peroxidase prior to the addition of primary antibodies. A 2-way staining protocol (biotin/horseradish peroxidase (HRP)) was used employing 3,3'-Diaminobenzidine (DAB) as a substrate. All sections were counterstained with heamatoxylin, washed and mounted with Entellan. Investigators were blinded to group allocations during both experiments and subsequent analyses.

Electron microscopy

Tissues were fixed in Karnovsky's fixative (2% paraformaldehyde, 2.5% glutaraldehyde in 0.1 M cacodylate buffer at pH 7.2). Post-fixation was performed with 1% osmiumtetroxide in 0.1 M cacodylate buffer at pH 7.2. After washing, tissue blocks were stained *en bloc* with Ultrastain 1 (Leica, Vienna, Austria), followed by ethanol dehydration series. Finally, tissue was embedded in a mixture of DDSA/NMA/Embed-812 (EMS, Hatfield, Pennsylvania, USA), sectioned and stained with Ultrastain 2 (Leica) and analyzed with a Tecnai 12G2 electron microscope (FEI, Eindhoven, Netherlands). Investigators were blinded to group allocations during the experiments and subsequent analyses.

Skin permeability assay

Newborn mice were euthanized though intraperitoneal administration of a lethal dose of anaesthetic. The tail of each pup was clipped and stored for PCR-based genotypic analysis. Carcasses were rinsed in ice-cold PBS and dehydrated by immersion in 25%, 50%, 75%, and 100% methanol for 2 minutes each at 4°C. Next, they were progressively rehydrated by immersion in 100%, 75%, 50% and 25% methanol for 2

minutes each at 4°C and finally in PBS. After immersion in 0.1% toluidine blue for 2 minutes on ice, carcasses were briefly washed in PBS and immediately photographed. PCR-based genotypic analyses were conducted only after completion of the assay. Investigators were blinded to group allocations during the experiments and subsequent analyses.

Standard biochemical procedures and antibodies

Cell lysates, protein quantification and SDS-PAGE were done as previously described (Beli et al., 2008; Galovic et al., 2011; Isogai et al., 2016; Isogai et al., 2015a). Fractionations were run on 4-15% gradient gels (TGX, Bio-rad) using the Laemmli buffer system and blotted on nitrocellulose (pore size 0.2 μm (Pall, USA)). Blots were routinely blocked with 5% BSA for 1 hour and then, depending on the manufacturer, incubated with primary antibodies for 1 hour or overnight. All secondary HPR-conjugated antibodies were from Bio-rad. Primary antibodies are listed in Table S4.

Immunofluorescence, imaging and image analysis

Keratinocytes were plated on collagen I (2 μg ml^{-1})-coated coverslips and treated 48 hours later. Cells were fixed as previously described (Isogai et al., 2015d) and images acquired sequentially on a CLSM Leica TCS SP5 using identical settings throughout each experiment. For confocal time-lapse video microscopy, cells were plated on collagen I-coated glass-bottom Cellview dishes (Greiner) and imaged on a CLSM Leica TCS SP5 microscope equipped with a humidified climate chamber with 5% CO_2 at 37°C (63x 1.45 N.A, Argon laser 5-7%, 1.4 A.U., line scan mode, accumulation 4, gain 40%, 2 frames min^{-1}). Movies were assembled from (512 x 512 pixels) time series and processed using ImageJ.

Automated analysis compressed confocal (1024 x 1024 pixel) Z-stacks of non-permeabilised EGFP-Nrf2-expressing keratinocytes counterstained with DAPI was carried out using Cell profiler (Broad Institute) (Jones et al., 2008) and a custom-modified "Human cytoplasm-nucleus translocation assay" pipeline.

Semi-quantitative analysis of Arpc4 immunoreactivity in human skin samples was performed as follows: images were processed using ImageJ plugin "IHC ToolBox" (https://imagej.nih.gov/ij/plugins/ihc-toolbox/index.html) using either preset or custom-made H-DAB models to extract the unmixed DAB (brown) signal. The

resulting DAB images were inspected manually and only those ensuring a satisfactory removal of the counterstaining were analyzed. For each image, two full-thickness epidermal ROIs were randomly selected and mean intensity measured with ImageJ "Measure" function. Values were averaged and then converted from the original 0-255 (black-white) scale into a 0-1 (black-white) scale. Each value (x) was then transformed using the 1-x formula for plotting according to a more intuitive 0-1 (white-black) scale.

Fractionations

To obtain cytosol-enriched and nuclear-enriched fractions, keratinocytes (approximately 16 x 10^6 cells, 80-percent confluent cultures) were washed twice with ice-cold PBS supplemented with Calcium and Magnesium, scraped with a rubber policeman and spun at 900 g for 5 minutes at 4°C. Pellet was taken up in 150 µl hypertonic buffer (100 mM PIPES pH 6.8, 1 mM EGTA, 1 mM $MgCl_2$ supplemented with phosphatase and protease inhibitor cocktail (Roche)), re-suspended gently and left at room temperature for 5 minutes. After addition of 0.5% Triton-X100 and gentle resuspension, samples were spun and centrifuged at 900 g for 5 minutes at 4°C. The resulting supernatant is referred to as cytosol. Instead, the pellet was washed with 10 bed volumes of hypertonic buffer without Triton-X100 and then resuspended in RIPA buffer (50 mM Tis-HCl pH 7.5, 150 mM NaCl, 1% NP-40, 0.5% Sodium deoxycholate, 0.1% SDS) supplemented with phosphatase and protease inhibitor cocktail (Roche), sonicated three times for 10 seconds in a Branson sonicator bath (75% intensity) and centrifuged for 30 minutes at 15,000 rpm at 4°C. The final supernatant is referred to as nucleus.

To obtain G-actin and F-actin fractions, the G-actin/F-actin in vivo assay kit (Cytoskeleton Inc.) was used. Briefly, keratinocytes (approximately 3 x 10^6 cells, 80-percent confluent cultures) were lysed in 400 µl of the LAS2 as per manufacturer's instructions. After removing cell debris and unbroken cells, protein concentration was measured and lysates diluted in LAS2 buffer to obtain a final concentration of 1 mg ml^{-1}. Next, 150 µl of each lysate were fractionated.

Muscle actin (Cytoskeleton Inc.) was recycled as previously described (Hertzog and Carlier, 2005) and then used for the F-actin co-sedimentation assays using an established protocol (Hertzog and Carlier, 2005). Full-length GST-Nrf2 was

expressed in *E. coli* and purified using previously described procedures (Beli et al., 2008; Galovic et al., 2011; Innocenti et al., 2005; Innocenti et al., 2004) with the exception that cell were grown at 30°C prior to induction.

Tissue homogenization, total RNA isolation, TruSeq Stranded mRNA sample preparation, sequencing and bioinformatics

Tissues were homogenized in TRIzol reagent (Ambion life technologies) using a polytron (DI 18 Disperser, IKA) as per manufacturer's protocol. Typically, 1 and 0.5 ml of TRIzol reagent were used per 50-100 mg of epidermis and 1 x 10^6 cells, respectively.

Total RNA was extracted using TRIzol reagent as per manufacturer's protocol. Briefly, 0.2 volumes of chloroform (Chloroform stab./Amylene, Biosolve) were added to the TRIzol homogenate and tube(s) (Falcon, 15 ml) were shaken vigorously. The tubes were incubated for 2-3 minutes at room temperature and centrifuged (Hettich, rotanta 46 RS) for 1 hour at 4°C. Approximately 70% of the upper aqueous phase was transferred to a clean 15 ml tube and 0.5 volumes of isopropanol (Sigma-Aldrich) were added. The tube(s) were then incubated overnight at -20°C and centrifuged for 30 minutes at 4°C. The supernatant was removed and the pellet was washed twice with 80% ethanol (Sigma-Aldrich). The total RNA pellet was air-dried for 8 minutes and dissolved in an appropriate volume of nuclease-free water (Ambion life technologies) and quantified using Nanodrop UV-VIS Spectrophotometer. The total RNA was further purified using MinElute Cleanup Kit (Qiagen) according to the manufacturer's instructions. Quality and quantity of the total RNA was assessed by the 2100 Bioanalyzer using a Nano chip (Agilent). Total RNA samples having RIN > 8 were subjected to library generation.

Strand-specific libraries were generated using the TruSeq Stranded mRNA sample preparation kit (Illumina Inc., RS-122-2101/2) according to the manufacturer's instructions (Illumina, Part # 15031047 Rev. E). Briefly, polyadenylated RNA from 1,000 ng intact total RNA was purified using oligo-dT beads. Following purification, RNA was fragmented, random primed and reverse transcribed using SuperScript II Reverse Transcriptase (Invitrogen, part # 18064-014) with the addition of Actinomycin D. Second strand synthesis was performed using Polymerase I and RNaseH with replacement of dTTP for dUTP. The generated cDNA fragments were 3'-end adenylated and ligated to Illumina Paired-end sequencing adapters and

subsequently amplified by 12 cycles of PCR. The libraries were analyzed on a 2100 Bioanalyzer using a 7500 chip (Agilent), diluted and pooled equimolar into a 10-plex, 10 nM sequencing pool.

The epidermal libraries were sequenced with 65-base single reads on a HiSeq2500 using V4 chemistry (Illumina Inc.). Reads were aligned with Tophat (Kim et al., 2013a; Trapnell et al., 2009) (version 2.0.12), which allows for exon-exon-junctions against the mouse build 38. Read counts were generated using a custom script based on the union mode of the HTSseq-count (Anders et al., 2015). Only reads that mapped uniquely to the transcriptome were used for counting. All samples were merged into one dataset and genes that have zero expression across all samples were removed from the dataset. Identification of differentially expressed genes was performed using the R package Limma (Ritchie et al., 2015). In Fig. 2, wild-type samples were compared against knockout samples and a given gene was considered differential expressed only when the p-value was < 0.05 in all three comparisons. In order to create a robust list, a Log_2 fold change of 1.5 was set as a minimum. Nrf2-target genes were retrieved from http://nrf2.elte.hu and, after removal of duplicated entries, complemented by mining Nrf2-target genes from published literature. The MRTF signature (921 genes) was previously published (Esnault et al., 2014). Investigators were blinded to group allocations during the experiments.

RT-qPCR

Total RNA was isolated from keratinocytes and skin epidermis using GeneJET RNA purification kit (Thermo scientific) and TRIzol, respectively. For keratinocytes, complementary DNA synthesis was performed using 1-2 µg of mRNA with High Capacity cDNA Reverse transcription Kit (Applied Biosystems) and oligo-dT (25 ng ml^{-1}) according to the manufacturer's instructions. For the epidermis, the mix was also supplemented with random primers (1:100 from the supplied 10x RT stock solution). Real-time qPCR reactions were set up using 1-2 ng of cDNA as a template and gene specific primers (600 nM) in a StepOnePlusTM Real-Time PCR system (Applied Biosystems). All reactions produced single amplicons (100-200 bp), which allowed us to equate one threshold cycle difference using Hprt as reference housekeeping gene (Isogai et al., 2015b). Biological duplicates were assayed in triplicate and data were normalized with respect to the central value of the control. RT-qPCR primers are listed in Table S5.

Collection and staining of human skin samples

Skin biopsies were taken from lesional skin of adult patients affected by chronic plaque psoriasis (n = 10). Biopsies were also obtained from normal skin of healthy subjects undergoing plastic surgery (n = 5). For six psoriatic patients, a skin biopsy from uninvolved normal-appearing skin distant from the lesions was also taken.

For immunohistochemistry, skin samples were fixed in 10% formalin and embedded in paraffin. Five-µm-thick sections were dewaxed and rehydrated. After quenching endogenous peroxidase, achieving antigen retrieval, and blocking non-specific binding sites, sections were incubated overnight at 4°C with goat anti-Arpc4 antibodies. Biotinylated anti-goat antibodies and staining kits were from Vector Laboratories. Signal was developed using DAB (3,3'-diaminobenzidine) (DAKO, Glostrum, Denmark) followed by counterstaining with hematoxylin (Vector Laboratories). Controls omitting the primary antibodies gave virtually no staining (not shown).

Statistics

GraphPad Prism (version 6.oh) was used to carry out all statistical analyses and to plot results as indicated in the figure legends.

Study approval

Animal studies were performed with approval of the local Animals Ethics Committee (DEC) and according to Dutch legislation. IMQ treatments were performed in compliance with a protocol approved by the Italian ISS (Istituto Superiore di Sanità) (23/12/2013, IDI protocol N. SA-IDI-CA-1). Human studies were performed according to the Declaration of Helsinki with regard to scientific use, and approved by the ethical committee of the Fondazione “Luigi Maria Monti” - Istituto Dermopatico dell’Immacolata (IDI)-IRCCS (Rome, Italy) (23/12/2015, Protocol N. 103/CE/2015). Patients were enrolled in the study after written informed consent.

Acknowledgments

We thank J. Neefjes (Leiden University) for the EGFP-Nrf2 plasmid, A. Berns (NKI) and A. Sonnenberg (NKI) for critical reading of the manuscript. We thank Ron Kerkhoven for supervising the work of the NKI Genomics Core Facility.

Competing interests

The authors declare no competing or financial interests.

Author contributions

R.V.D.K. and M.I. performed and analyzed experiments, J.Y.S. carried out pathological analyses, W.B. and I.D.R. performed the RNAseq and associated bioinformatics, respectively, H.J. generated and analyzed the EM images, S.M., C.S. and C.A. generated and studied the IMQ-induced mouse model of psoriasis, stained and analyzed the human skin biopsies. M.I. conceived the project, coordinated the work and wrote the manuscript.

Supplementary information

Supplementary information available online and consists of nine figures, two movies and five tables.

REFERENCES

Abella, J. V., Galloni, C., Pernier, J., Barry, D. J., Kjaer, S., Carlier, M. F. and Way, M. (2016). Isoform diversity in the Arp2/3 complex determines actin filament dynamics. *Nat Cell Biol* **18**, 76-86.

Anders, S., Pyl, P. T. and Huber, W. (2015). HTSeq--a Python framework to work with high-throughput sequencing data. *Bioinformatics* **31**, 166-169.

Beli, P., Mascheroni, D., Xu, D. and Innocenti, M. (2008). WAVE and Arp2/3 jointly inhibit filopodium formation by entering into a complex with mDia2. *Nat Cell Biol* **10**, 849-857.

Bose, A., Teh, M. T., Mackenzie, I. C. and Waseem, A. (2013). Keratin k15 as a biomarker of epidermal stem cells. *Int J Mol Sci* **14**, 19385-19398.

Eisenmann, K. M., West, R. A., Hildebrand, D., Kitchen, S. M., Peng, J., Sigler, R., Zhang, J., Siminovitch, K. A. and Alberts, A. S. (2007). T cell responses in mammalian diaphanous-related formin mDia1 knock-out mice. *J Biol Chem* **282**, 25152-25158.

Esnault, C., Stewart, A., Gualdrini, F., East, P., Horswell, S., Matthews, N. and Treisman, R. (2014). Rho-actin signaling to the MRTF coactivators dominates the immediate transcriptional response to serum in fibroblasts. *Genes Dev* **28**, 943-958.

Galovic, M., Xu, D., Areces, L. B., van der Kammen, R. and Innocenti, M. (2011). Interplay between N-WASP and CK2 optimizes clathrin-mediated endocytosis of EGFR. *J Cell Sci* **124**, 2001-2012.

Goley, E. D. and Welch, M. D. (2006). The ARP2/3 complex: an actin nucleator comes of age. *Nat Rev Mol Cell Biol* **7**, 713-726.

Gorrini, C., Harris, I. S. and Mak, T. W. (2013). Modulation of oxidative stress as an anticancer strategy. *Nat Rev Drug Discov* **12**, 931-947.

Gournier, H., Goley, E. D., Niederstrasser, H., Trinh, T. and Welch, M. D. (2001). Reconstitution of human Arp2/3 complex reveals critical roles of individual subunits in complex structure and activity. *Mol Cell* **8**, 1041-1052.

Hertzog, M. and Carlier, M. F. (2005). Functional characterization of proteins regulating actin assembly. *Curr Protoc Cell Biol* **Chapter 13**, Unit 13 16.

Hotulainen, P. and Lappalainen, P. (2006). Stress fibers are generated by two distinct actin assembly mechanisms in motile cells. *J Cell Biol* **173**, 383-394.

Huang, H. C., Nguyen, T. and Pickett, C. B. (2002). Phosphorylation of Nrf2 at Ser-40 by protein kinase C regulates antioxidant response element-mediated transcription. *J Biol Chem* **277**, 42769-42774.

Huelsken, J., Vogel, R., Erdmann, B., Cotsarelis, G. and Birchmeier, W. (2001). beta-Catenin controls hair follicle morphogenesis and stem cell differentiation in the skin. *Cell* **105**, 533-545.

Innocenti, M., Gerboth, S., Rottner, K., Lai, F. P., Hertzog, M., Stradal, T. E., Frittoli, E., Didry, D., Polo, S., Disanza, A., et al. (2005). Abi1 regulates the activity of N-WASP and WAVE in distinct actin-based processes. *Nat Cell Biol* **7**, 969-976.

Innocenti, M., Zucconi, A., Disanza, A., Frittoli, E., Areces, L. B., Steffen, A., Stradal, T. E., Di Fiore, P. P., Carlier, M. F. and Scita, G. (2004). Abi1 is essential for the formation and activation of a WAVE2 signalling complex. *Nat Cell Biol* **6**, 319-327.

Isogai, T., van der Kammen, R., Bleijerveld, O. B., Goerdayal, S. S., Argenzio, E., Altelaar, A. F. and Innocenti, M. (2016). Quantitative Proteomics Illuminates a Functional Interaction between mDia2 and the Proteasome. *J Proteome Res* **15**, 4624-4637.

Isogai, T., van der Kammen, R., Goerdayal, S. S., Heck, A. J., Altelaar, A. F. and Innocenti, M. (2015a). Proteomic analyses uncover a new function and mode of action for mouse homolog of Diaphanous 2 (mDia2). *Mol Cell Proteomics* **14**, 1064-1078.

Isogai, T., van der Kammen, R. and Innocenti, M. (2015b). SMIFH2 has effects on Formins and p53 that perturb the cell cytoskeleton. *Scientific reports* **5**, 9802.

Isogai, T., van der Kammen, R., Leyton-Puig, D., Kedziora, K. M., Jalink, K. and Innocenti, M. (2015d). Initiation of lamellipodia and ruffles involves cooperation between mDia1 and the Arp2/3 complex. *J Cell Sci* **128**, 3796-3810.

Jones, T. R., Kang, I. H., Wheeler, D. B., Lindquist, R. A., Papallo, A., Sabatini, D. M., Golland, P. and Carpenter, A. E. (2008). CellProfiler Analyst: data exploration and analysis software for complex image-based screens. *BMC Bioinformatics* **9**, 482.

Kang, M. I., Kobayashi, A., Wakabayashi, N., Kim, S. G. and Yamamoto, M. (2004). Scaffolding of Keap1 to the actin cytoskeleton controls the function of

Nrf2 as key regulator of cytoprotective phase 2 genes. *Proc Natl Acad Sci U S A* **101**, 2046-2051.

Kim, D., Pertea, G., Trapnell, C., Pimentel, H., Kelley, R. and Salzberg, S. L. (2013a). TopHat2: accurate alignment of transcriptomes in the presence of insertions, deletions and gene fusions. *Genome biology* **14**, R36.

Kim, I. H., Racz, B., Wang, H., Burianek, L., Weinberg, R., Yasuda, R., Wetsel, W. C. and Soderling, S. H. (2013b). Disruption of Arp2/3 results in asymmetric structural plasticity of dendritic spines and progressive synaptic and behavioral abnormalities. *J Neurosci* **33**, 6081-6092.

Kim, I. H., Rossi, M. A., Aryal, D. K., Racz, B., Kim, N., Uezu, A., Wang, F., Wetsel, W. C., Weinberg, R. J., Yin, H., et al. (2015). Spine pruning drives antipsychotic-sensitive locomotion via circuit control of striatal dopamine. *Nature neuroscience* **18**, 883-891.

Kim, W., Bennett, E. J., Huttlin, E. L., Guo, A., Li, J., Possemato, A., Sowa, M. E., Rad, R., Rush, J., Comb, M. J., et al. (2011). Systematic and quantitative assessment of the ubiquitin-modified proteome. *Mol Cell* **44**, 325-340.

Kobielak, A., Pasolli, H. A. and Fuchs, E. (2004). Mammalian formin-1 participates in adherens junctions and polymerization of linear actin cables. *Nat Cell Biol* **6**, 21-30.

Kobielak, K., Pasolli, H. A., Alonso, L., Polak, L. and Fuchs, E. (2003). Defining BMP functions in the hair follicle by conditional ablation of BMP receptor IA. *J Cell Biol* **163**, 609-623.

Koch, P. J., de Viragh, P. A., Scharer, E., Bundman, D., Longley, M. A., Bickenbach, J., Kawachi, Y., Suga, Y., Zhou, Z., Huber, M., et al. (2000). Lessons from loricrin-deficient mice: compensatory mechanisms maintaining skin barrier function in the absence of a major cornified envelope protein. *J Cell Biol* **151**, 389-400.

Leyton-Puig, D., Isogai, T., Argenzio, E., van den Broek, B., Klarenbeek, J., Janssen, H., Jalink, K. and Innocenti, M. (2017). Flat clathrin lattices are dynamic actin-controlled hubs for clathrin-mediated endocytosis and signalling of specific receptors. *Nature communications* **8**, 16068.

Margadant, C., Raymond, K., Kreft, M., Sachs, N., Janssen, H. and Sonnenberg, A. (2009). Integrin alpha3beta1 inhibits directional migration and wound re-epithelialization in the skin. *J Cell Sci* **122**, 278-288.

Matsuki, M., Yamashita, F., Ishida-Yamamoto, A., Yamada, K., Kinoshita, C., Fushiki, S., Ueda, E., Morishima, Y., Tabata, K., Yasuno, H., et al. (1998). Defective stratum corneum and early neonatal death in mice lacking the gene for transglutaminase 1 (keratinocyte transglutaminase). *Proc Natl Acad Sci U S A* **95**, 1044-1049.

Mertens, A. E., Rygiel, T. P., Olivo, C., van der Kammen, R. and Collard, J. G. (2005). The Rac activator Tiam1 controls tight junction biogenesis in keratinocytes through binding to and activation of the Par polarity complex. *J Cell Biol* **170**, 1029-1037.

Michelot, A. and Drubin, D. G. (2011). Building distinct actin filament networks in a common cytoplasm. *Curr Biol* **21**, R560-569.

Nolen, B. J., Tomasevic, N., Russell, A., Pierce, D. W., Jia, Z., McCormick, C. D., Hartman, J., Sakowicz, R. and Pollard, T. D. (2009). Characterization of two classes of small molecule inhibitors of Arp2/3 complex. *Nature* **460**, 1031-1034.

Palombo, R., Savini, I., Avigliano, L., Madonna, S., Cavani, A., Albanesi, C., Mauriello, A., Melino, G. and Terrinoni, A. (2016). Luteolin-7-glucoside inhibits IL-22/STAT3 pathway, reducing proliferation, acanthosis, and inflammation in keratinocytes and in mouse psoriatic model. *Cell Death Dis* **7**, e2344.

Papp, D., Lenti, K., Modos, D., Fazekas, D., Dul, Z., Turei, D., Foldvari-Nagy, L., Nussinov, R., Csermely, P. and Korcsmaros, T. (2012). The NRF2-related interactome and regulome contain multifunctional proteins and fine-tuned autoregulatory loops. *FEBS Lett* **586**, 1795-1802.

Posern, G. and Treisman, R. (2006). Actin' together: serum response factor, its cofactors and the link to signal transduction. *Trends Cell Biol* **16**, 588-596.

Raymond, K., Kreft, M., Janssen, H., Calafat, J. and Sonnenberg, A. (2005). Keratinocytes display normal proliferation, survival and differentiation in conditional beta4-integrin knockout mice. *J Cell Sci* **118**, 1045-1060.

Ritchie, M. E., Phipson, B., Wu, D., Hu, Y., Law, C. W., Shi, W. and Smyth, G. K. (2015). limma powers differential expression analyses for RNA-sequencing and microarray studies. *Nucleic Acids Res* **43**, e47.

Roth, W., Kumar, V., Beer, H. D., Richter, M., Wohlenberg, C., Reuter, U., Thiering, S., Staratschek-Jox, A., Hofmann, A., Kreusch, F., et al. (2012).

Keratin 1 maintains skin integrity and participates in an inflammatory network in skin through interleukin-18. *J Cell Sci* **125**, 5269-5279.

Rotty, J. D., Wu, C. and Bear, J. E. (2013). New insights into the regulation and cellular functions of the ARP2/3 complex. *Nat Rev Mol Cell Biol* **14**, 7-12.

Schafer, M., Farwanah, H., Willrodt, A. H., Huebner, A. J., Sandhoff, K., Roop, D., Hohl, D., Bloch, W. and Werner, S. (2012). Nrf2 links epidermal barrier function with antioxidant defense. *EMBO Mol Med* **4**, 364-379.

Schafer, M. and Werner, S. (2015). Nrf2--A regulator of keratinocyte redox signaling. *Free Radic Biol Med* **88**, 243-252.

Schafer, M., Willrodt, A. H., Kurinna, S., Link, A. S., Farwanah, H., Geusau, A., Gruber, F., Sorg, O., Huebner, A. J., Roop, D. R., et al. (2014). Activation of Nrf2 in keratinocytes causes chloracne (MADISH)-like skin disease in mice. *EMBO Mol Med* **6**, 442-457.

Schulze-Topphoff, U., Varrin-Doyer, M., Pekarek, K., Spencer, C. M., Shetty, A., Sagan, S. A., Cree, B. A., Sobel, R. A., Wipke, B. T., Steinman, L., et al. (2016). Dimethyl fumarate treatment induces adaptive and innate immune modulation independent of Nrf2. *Proc Natl Acad Sci U S A* **113**, 4777-4782.

Segre, J. A. (2006). Epidermal barrier formation and recovery in skin disorders. *The Journal of clinical investigation* **116**, 1150-1158.

Simpson, C. L., Patel, D. M. and Green, K. J. (2011). Deconstructing the skin: cytoarchitectural determinants of epidermal morphogenesis. *Nat Rev Mol Cell Biol* **12**, 565-580.

Sotiropoulou, P. A. and Blanpain, C. (2012). Development and homeostasis of the skin epidermis. *Cold Spring Harbor perspectives in biology* **4**, a008383.

Stradal, T. E., Rottner, K., Disanza, A., Confalonieri, S., Innocenti, M. and Scita, G. (2004). Regulation of actin dynamics by WASP and WAVE family proteins. *Trends Cell Biol* **14**, 303-311.

Sykiotis, G. P. and Bohmann, D. (2010). Stress-activated cap'n'collar transcription factors in aging and human disease. *Sci Signal* **3**, re3.

Trapnell, C., Pachter, L. and Salzberg, S. L. (2009). TopHat: discovering splice junctions with RNA-Seq. *Bioinformatics* **25**, 1105-1111.

Vaezi, A., Bauer, C., Vasioukhin, V. and Fuchs, E. (2002). Actin cable dynamics and Rho/Rock orchestrate a polarized cytoskeletal architecture in the early steps of assembling a stratified epithelium. *Dev Cell* **3**, 367-381.

van der Fits, L., Mourits, S., Voerman, J. S., Kant, M., Boon, L., Laman, J. D., Cornelissen, F., Mus, A. M., Florencia, E., Prens, E. P., et al. (2009). Imiquimod-induced psoriasis-like skin inflammation in mice is mediated via the IL-23/IL-17 axis. *J Immunol* **182**, 5836-5845.

Velichkova, M., Guttman, J., Warren, C., Eng, L., Kline, K., Vogl, A. W. and Hasson, T. (2002). A human homologue of Drosophila kelch associates with myosin-VIIa in specialized adhesion junctions. *Cell Motil Cytoskeleton* **51**, 147-164.

Velichkova, M. and Hasson, T. (2005). Keap1 regulates the oxidation-sensitive shuttling of Nrf2 into and out of the nucleus via a Crm1-dependent nuclear export mechanism. *Mol Cell Biol* **25**, 4501-4513.

Watt, F. M. (2014). Mammalian skin cell biology: at the interface between laboratory and clinic. *Science* **346**, 937-940.

Wynshaw-Boris, A., Ryan, G., Deng, C. X., Chan, D. C., Jackson-Grusby, L., Larson, D., Dunmore, J. H. and Leder, P. (1997). The role of a single formin isoform in the limb and renal phenotypes of limb deformity. *Mol Med* **3**, 372-384.

Yang, L., Fan, X., Cui, T., Dang, E. and Wang, G. (2017). Nrf2 promotes keratinocyte proliferation in psoriasis through up-regulation of Keratin 6, Keratin 16 and Keratin 17. *The Journal of investigative dermatology*.

Zhou, K., Muroyama, A., Underwood, J., Leylek, R., Ray, S., Soderling, S. H. and Lechler, T. (2013). Actin-related protein2/3 complex regulates tight junctions and terminal differentiation to promote epidermal barrier formation. *Proc Natl Acad Sci U S A* **110**, E3820-3829.

Zhou, K., Sumigray, K. D. and Lechler, T. (2015). The Arp2/3 complex has essential roles in vesicle trafficking and transcytosis in the mammalian small intestine. *Mol Biol Cell* **26**, 1995-2004.

Zuchero, J. B., Fu, M. M., Sloan, S. A., Ibrahim, A., Olson, A., Zaremba, A., Dugas, J. C., Wienbar, S., Caprariello, A. V., Kantor, C., et al. (2015). CNS myelin wrapping is driven by actin disassembly. *Dev Cell* **34**, 152-167.

Figures

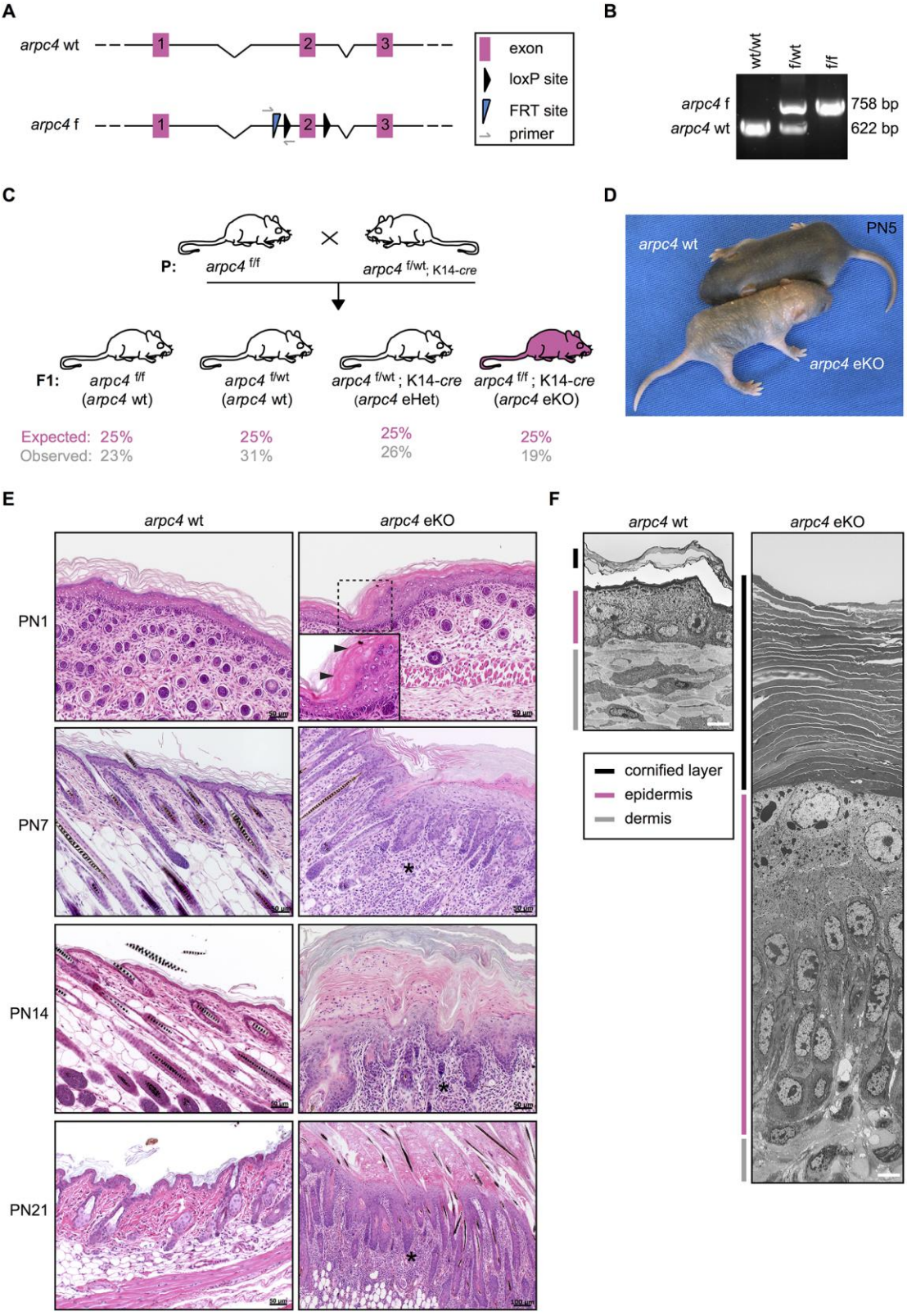

Fig. 1. *arpc4*$^{f/f}$*::K14*-Cre(neo) mice are viable and develop a psoriasis-like disease. (A) Schematic representation of the first three exons of wild-type (wt) and mutant (f, flox) *arpc4* locus. Exons are depicted approximately in scale and box decodes symbols. (B) Representative wild-type PCR showing the amplicons obtained from the wild-type (wt) and floxed (f) *arpc4* alleles. Location of forward and reverse primers is shown in A, size (bp = base pairs) of the wild-type and floxed amplicons is indicated on the right. (C) Breeding scheme showing the genotype of parents (P) and offspring (F1). Expected and observed mendelian ratios are indicated below each genotype. (eHet and eKO indicates that one and two *arpc4* f alleles underwent CRE-mediated recombination in the epidermis, respectively). Differences are not statistically significant (n = 86 mice). (D) Phenotype of *arpc4* wild-type (wt) and *arpc4* eKO pups at day 5 after birth. *arpc4* wild-type and *arpc4* eHet pups were undistinguishable (not shown). (E) Histochemical analysis of the skin of *arpc4* wt and *arpc4* eKO mice. Representative skin sections of *arpc4* wt and *arpc4* eKO mice at post-natal day (PN)1, 7, 14 and 21 are shown. Bar is 100 μm in the *arpc4* eKO panel at PN21 and 50 μm in all the other panels. Inset at PN1 depicts ghost cells highlighted by arrowheads. Asterisks mark dermis with massive immune infiltrates. (F) Ultrastructural analysis of the skin of *arpc4* wt and *arpc4* eKO mice at PN14. Images depict representative skin sections. Colours are decoded in the box. Bar is 4 μm.

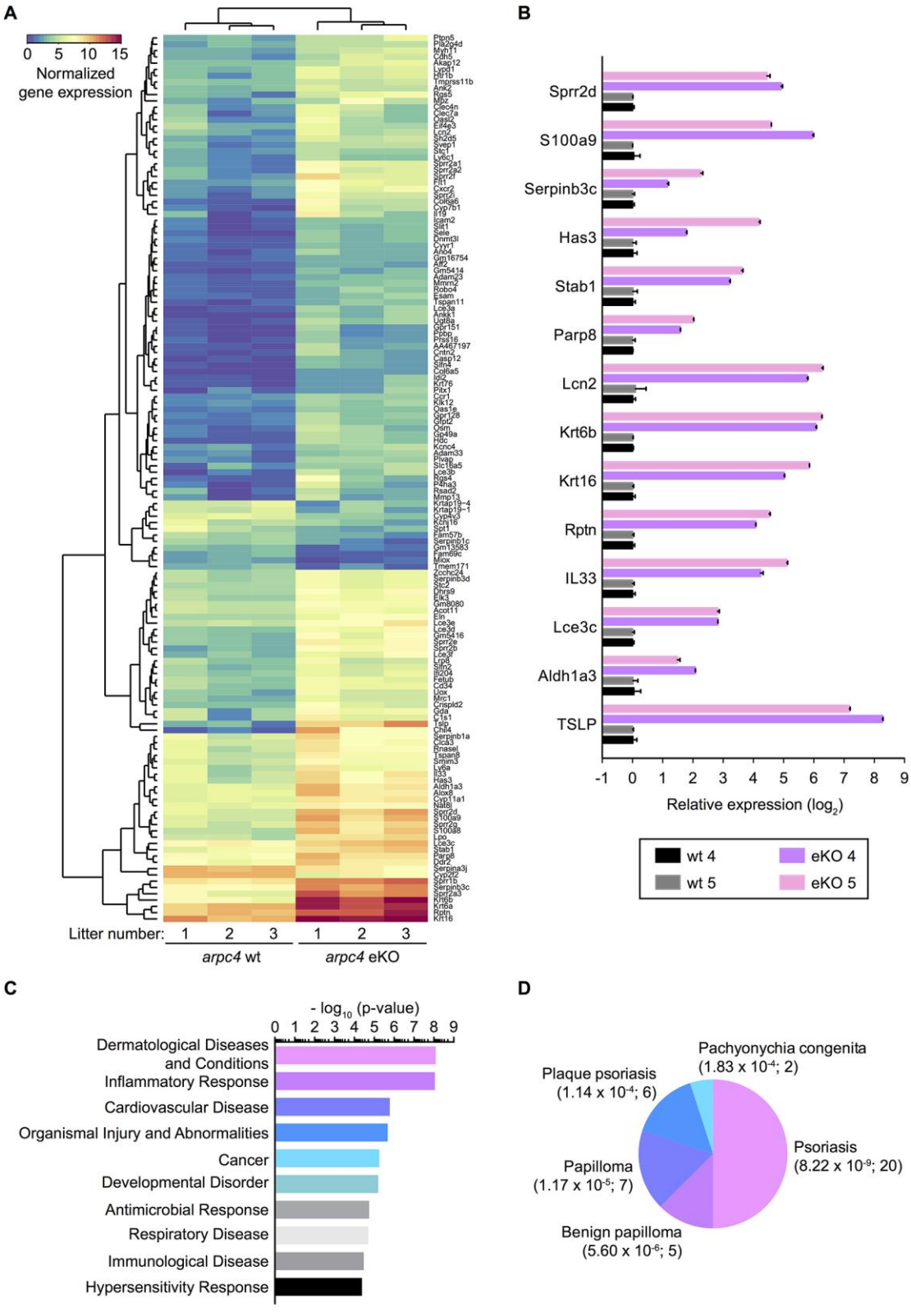

Fig. 2. Next generation sequencing reveals that the epidermis of the *arpc4* eKO mice displays a psoriasis-like gene expression profile.

(A) The Arp2/3 complex controls gene expression in the epidermis. Heat map of the 141 genes that are differentially expressed in the epidermis of *arpc4* wt and *arpc4* eKO mice. Epidermises of *arpc4* wt and *arpc4* eKO littermates taken from three different nests (litter number indicated below each column) were isolated at PN3-5 and processed for RNA sequencing. Genes showing at least a Log_2 fold change > 1.5 and a *p* value < 0.05 in all comparisons were classified as differentially expressed genes. Heat map depicts the normalized gene expression of the 141 differentially expressed genes according to the colour code indicated in the top-left bar. (B) Validation of the psoriasis-like gene expression profile. Total RNA isolated from the epidermis of two *arpc4* wt and *arpc4* eKO littermates (litter number indicated in the box) was used to compare the relative expression of the indicated genes by RT-qPCR. Data are expressed as mean and SEM and plotted using a Log_2 scale. (C) Top ten disease and pathological categories obtained from IPA of the annotated differentially expressed genes. Enrichment *p* values (p-value) are plotted using $-Log_{10}$ scale. (D) Pie chart showing the Diseases or Functions Annotation belonging to the Dermatological Diseases and Conditions category. Brackets report *p* values and number of identified genes.

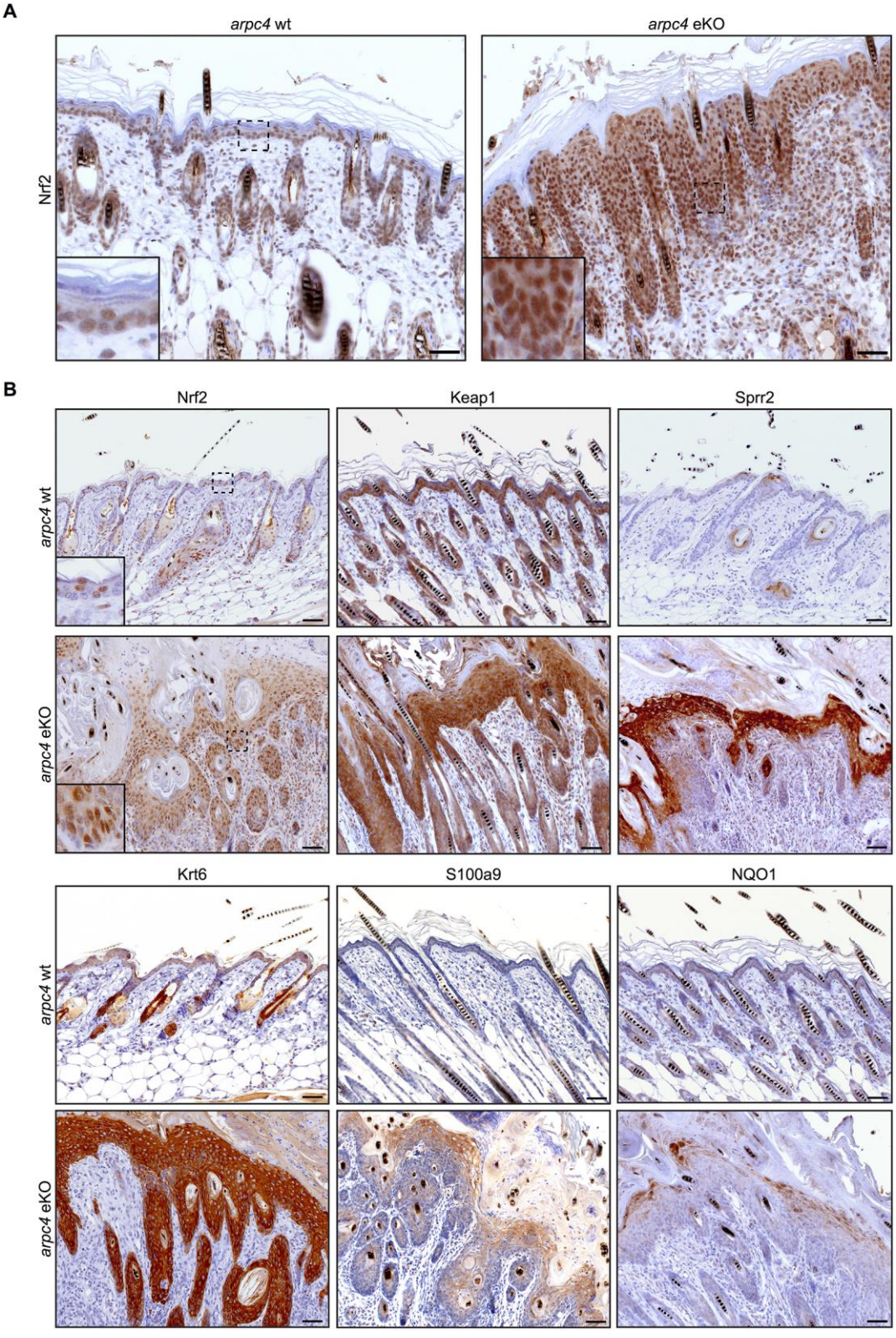

Fig. 3. Ablation of the Arp2/3 complex in the epidermis results in Nrf2 hyperactivation.

(A) Expression of Nrf2 in the epidermis of *arpc4* wt and *arpc4* eKO littermates at PN4. Images depict representative skin sections and dashed boxes mark zoomed-in regions. Bar is 50 μm. (B) Immunohistochemical characterization of the skin of *arpc4* wt and *arpc4* eKO littermates at PN14. Representative images show normal skin (*arpc4* wt) and psoriasis-like lesions (*arpc4* eKO) stained as indicated. Dashed boxes mark zoomed-in regions. Bar is 50 μm.

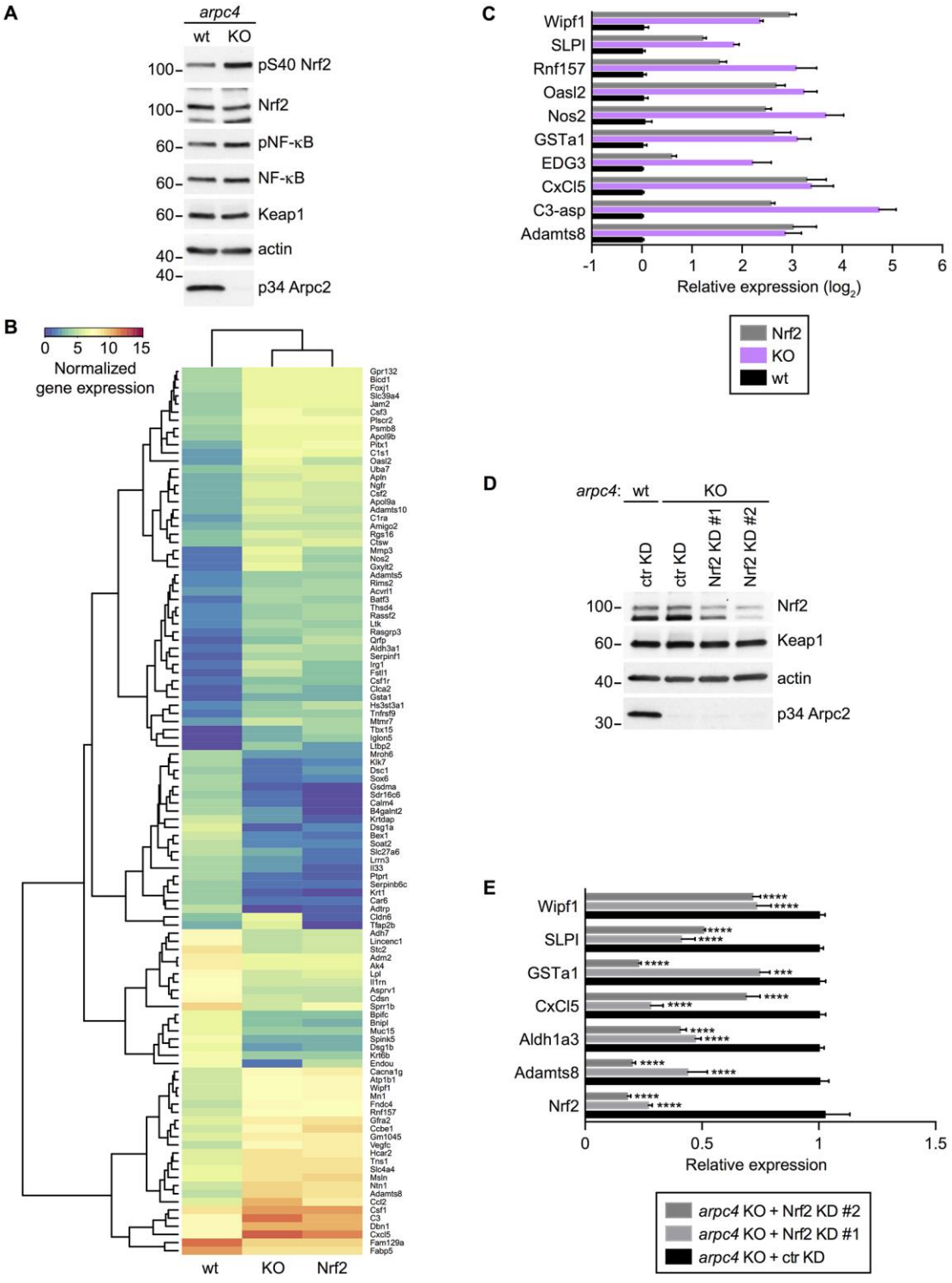

Fig. 4. Increased expression of Nrf2-target genes in *arpc4* knockout keratinocytes depends on Nrf2.

(A) Characterization of *arpc4* wild-type and knockout keratinocytes. Total cell lysates (30 μg) obtained from wild-type (wt) and knockout (KO) keratinocytes were blotted as indicated. Data are representative of two independent experiments. (B) Arp2/3 KO

and Nrf2-overexpressing keratinocytes display a similar gene expression profile. Transcriptome of wild-type (wt) keratinocytes was compared to that of *arpc4* KO (KO) and Nrf2-overexpressing (Nrf2) keratinocytes. Genes showing Log_2 fold change > 2 and *p* value < 0.05 in both comparisons were classified as differentially expressed. Heat map depicts the normalized gene expression of the 109 differentially expressed genes, colour-coded as indicated in the bar. (C) Validation of the gene expression profile. Relative expression of the indicated genes in the above keratinocyte lines was compared by RT-qPCR. Data representing mean and SEM (n = 6 from two independent experiments) are plotted using a Log_2 scale. (D) Silencing of Nrf2 in the *arpc4* knockout keratinocytes. We generated two independent Nrf2 knockdown (Nrf2 KD #1 and Nrf2 KD #2) *arpc4* knockout (KO) keratinocytes and used control knockdown (ctr KD) *arpc4* wt and KO cells as a reference. Total cell lysates (30 μg) were blotted as indicated. Data are representative of two independent experiments. The lower band in the Nrf2 blot is due to either cross-reacting proteins or Nrf2 degradation products. (E) Knockdown of Nrf2 attenuates the expression of Nrf2-target genes in the *arpc4* KO keratinocytes. Relative expression of the indicated genes in ctr KD and Nrf2 KD (#1 and #2) *arpc4* KO keratinocytes was compared by RT-qPCR. Data are expressed as mean and SEM (n ≥ 6 from at least two independent experiments; *** = $p < 0.001$; **** = $p < 0.0001$, One-way ANOVA with Bonferroni's correction for multiple comparisons).

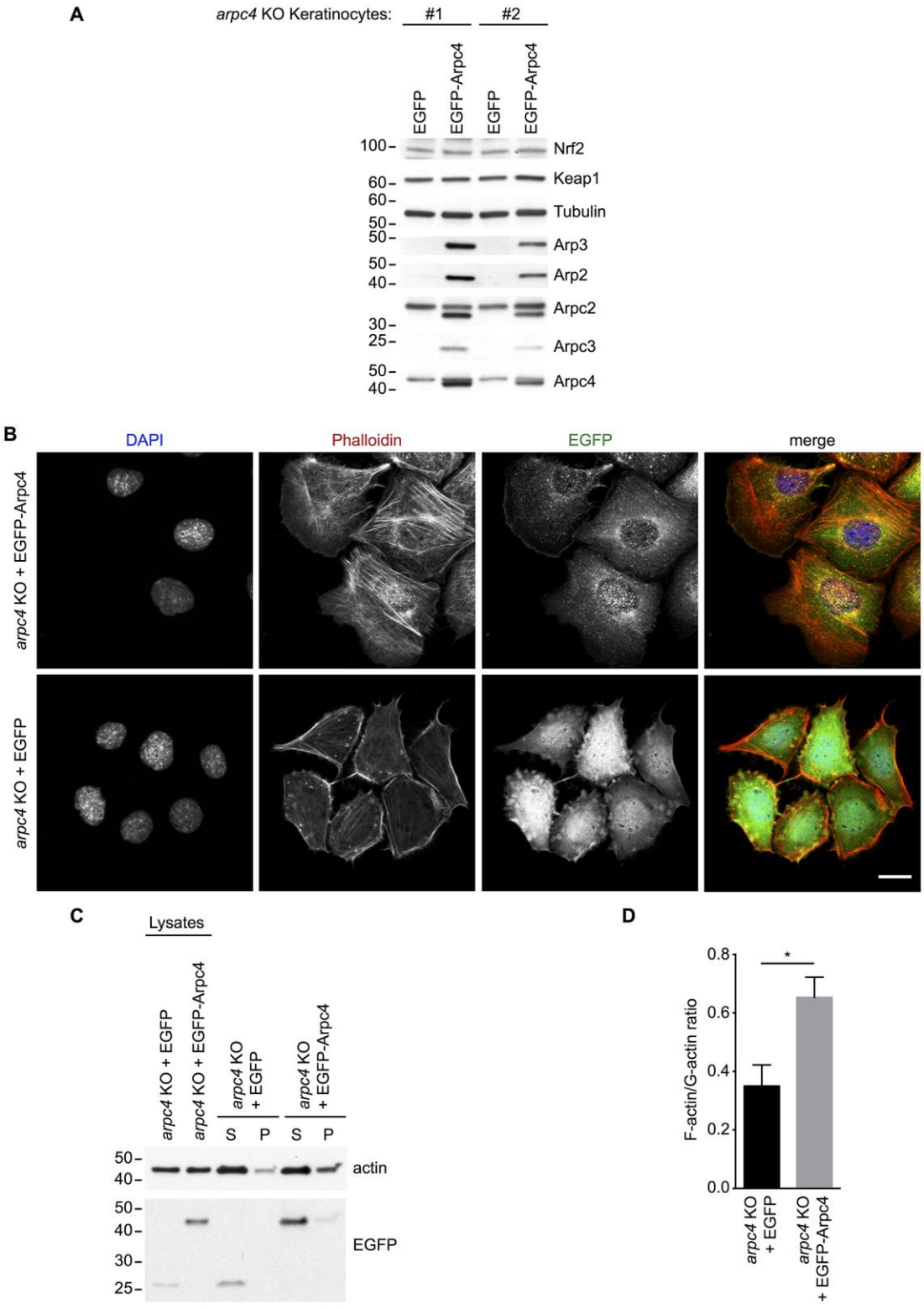

Fig. 5. Isogenic *arpc4* knockout and rescued keratinocytes show that the Arp2/3 complex regulates cell shape, formation of lamellipodia and F-actin content.

(A) Characterization of isogenic *arpc4* knockout and rescued keratinocytes. Independent lines of *arpc4* knockout (KO) keratinocytes (#1 and #2) were transduced

with retroviruses encoding either EGFP or EGFP-tagged Arpc4. Total cell lysates (30 μg) were blotted as indicated. Note that EGFP-Arpc4 migrates at about 45 kDa below a non-specific band. Data are representative of three independent experiments. (B) The *arpc4* knockout keratinocytes are smaller and do not form either lamellipodia or ruffles. Isogenic *arpc4* KO + EGFP and *arpc4* KO + EGFP-Arpc4 (line #1) were plated on collagen I-coated coverslips, fixed and processed in parallel, and imaged using identical settings. Representative compressed confocal Z-stacks show nuclei (DAPI, blue in merge), actin cytoskeleton (Phalloidin, red in merge) and either EGFP or EGFP-Arpc4 (EGFP, green in merge). Bar is 20 μm. Data are representative of three independent experiments. Line #2 gave similar results (see Fig. S3A). (C) Distribution of G-actin and F-actin in isogenic Arp2/3-complex knockout and rescued keratinocytes. *arpc4* KO + EGFP and *arpc4* KO + EGFP-Arpc4 keratinocytes (line #1) were plated on collagen I-coated dishes, harvested and lysed for separating G-actin from F-actin. Total cell lysates (30 μg) and the same percentage of soluble (S) and pelleted (P) material were blotted as indicated. Data are representative of three independent experiments. Line #2 gave similar results (see Fig. S3B). (D) The Arp2/3 complex knockout keratinocytes have less F-actin. Bar graph shows mean and SEM of the F-actin/G-actin ratio (densitometric intensity of actin in P *vs.* densitometric intensity of actin in S) in the *arpc4* KO + EGFP and the *arpc4* KO + EGFP-Arpc4 keratinocytes (line #1) (* = $p < 0.05$, unpaired two-tail t-test, n = 3).

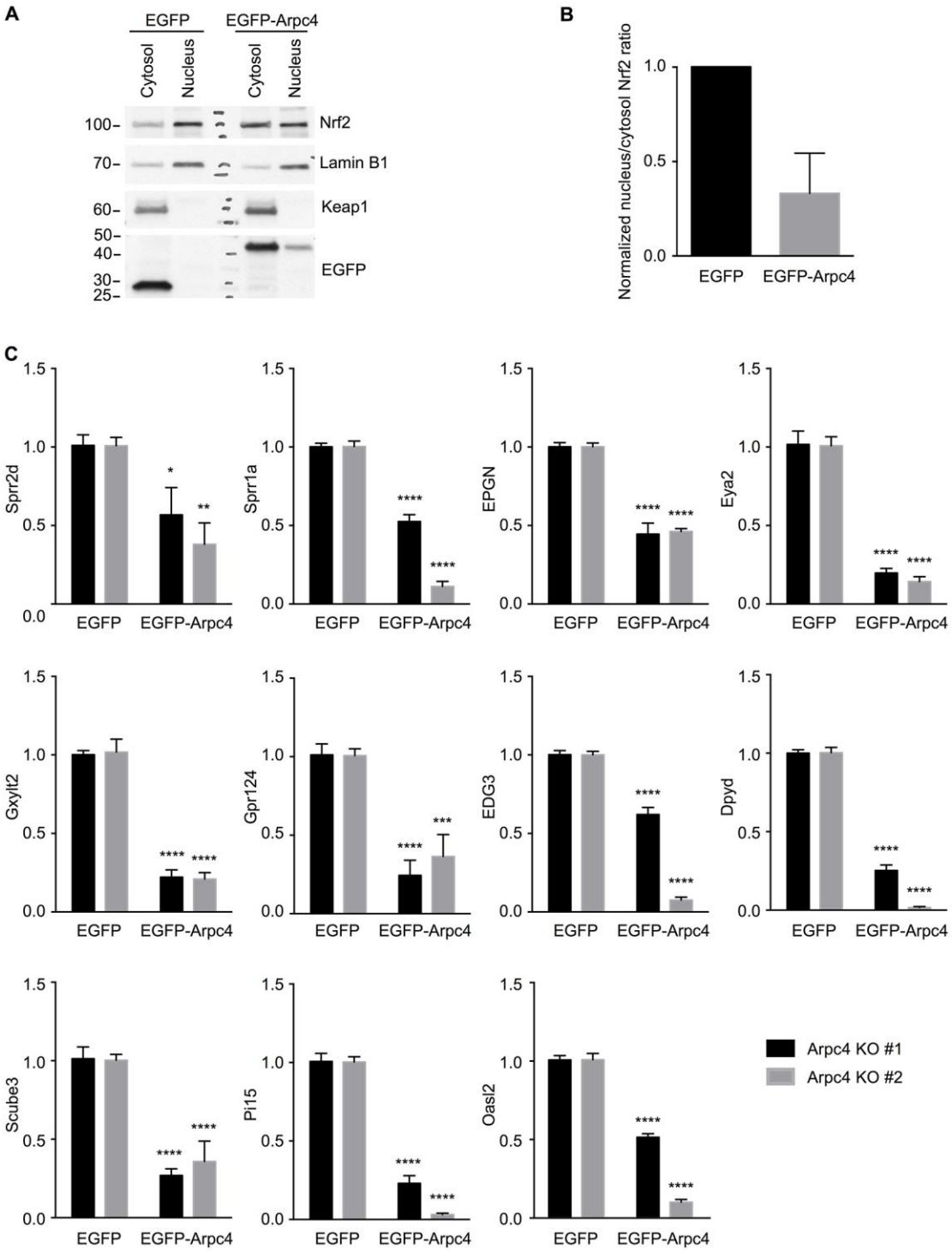

Fig. 6. The Arp2/3 complex controls the localization of Nrf2 and the expression of Nrf2-target genes in a cell-autonomous manner.

(A) The Arp2/3 complex controls the partitioning of Nrf2 between nucleus and cytosol. *arpc4* KO + EGFP and the *arpc4* KO + EGFP-Arpc4 keratinocytes (line #1) were plated on collagen I-coated dishes, harvested, lysed and fractionated to obtain cytosol-enriched (Cytosol) and nuclear-enriched (Nucleus) fractions. Equal

percentage (10% of the total volume) of either fraction was blotted as indicated. Data are representative of two independent experiments. (B) The Arp2/3 complex restrains Nrf2 into the cytosol. Bar graph shows mean and SD of the normalized nucleus/cytosol Nrf2 ratio in the *arpc4* KO + EGFP and the *arpc4* KO + EGFP-Arpc4 keratinocytes (line #1) (n = 2). The intensity of Nrf2 was determined by densitometry from non-saturated exposures. Values were normalized with respect to the ratio measured in the *arpc4* KO + EGFP cells. (C) The Arp2/3 complex controls the expression of Nrf2-target genes. Total RNA isolated from the *arpc4* KO + EGFP and the *arpc4* KO + EGFP-Arpc4 keratinocytes (line #1 in black, line #2 in and grey) was used to compare the relative expression of the indicated genes by RT-qPCR. Data are expressed as mean and SEM (n ≥ 6 from at least two independent experiments; * = $p < 0.05$; ** = $p < 0.01$; **** = $p < 0.0001$, Two-way ANOVA).

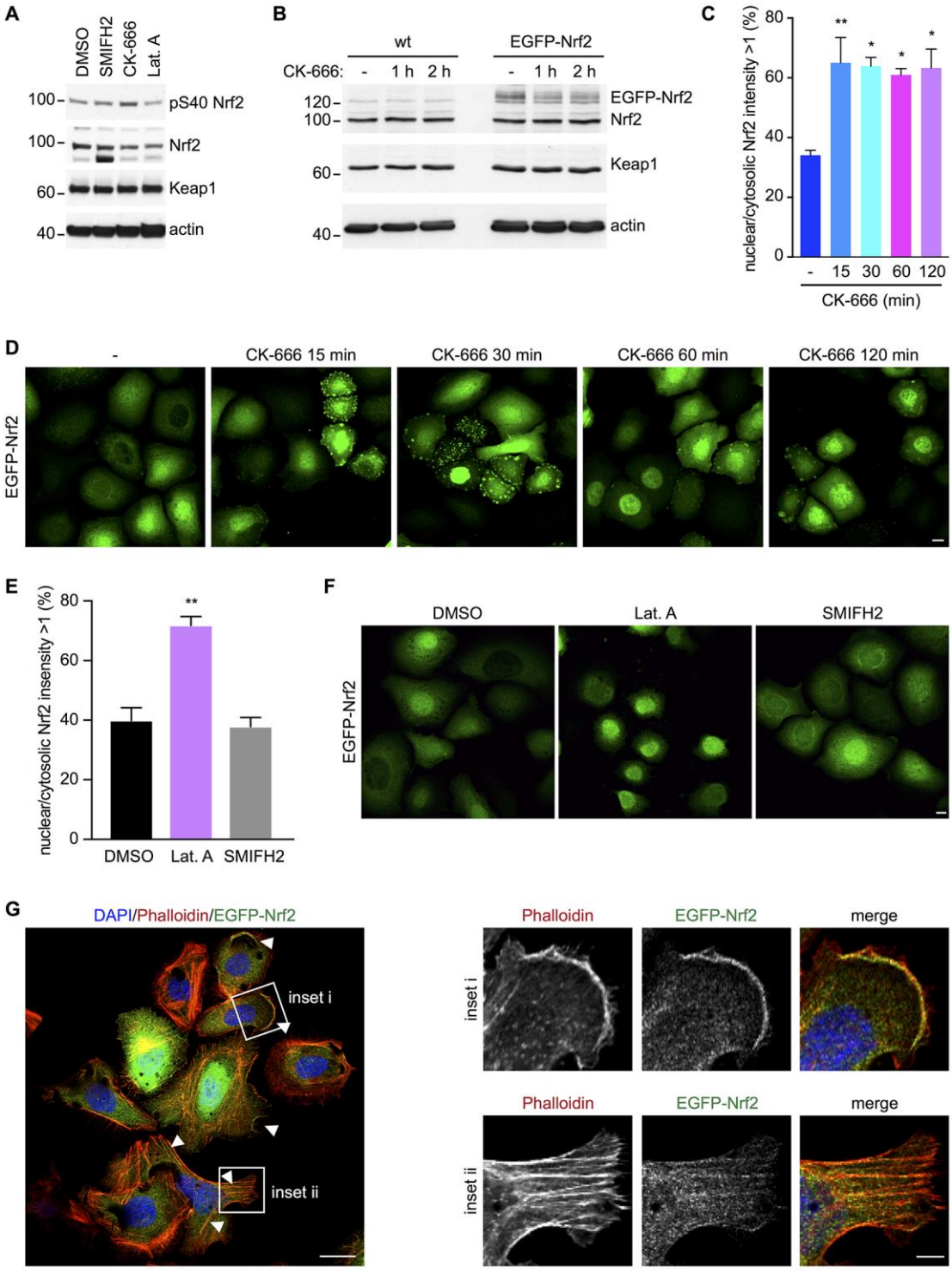

Fig. 7. Inhibition of the Arp2/3 complex triggers nuclear translocation of Nrf2, which partially localizes on actin filaments.

(A) Inhibition of the Arp2/3 complex increases the phosphorylation of Nrf2 at Ser40. Wild-type keratinocytes were plated on collagen I-coated dishes and treated with DMSO (-), or SMIFH2 (3 μM), or CK-666 (100 μM), or Latrunculin A (Lat. A, 0.25

μM) for 60 minutes. Total cell lysates (30 μg) were blotted as indicated. (B) Nrf2 expression levels in wild-type and EGFP-Nrf2-expressing keratinocytes. Wild-type (wt) and EGFP-Nrf2-expressing keratinocytes were plated on collagen I-coated dishes and treated with CK-666 (100 μM) or DMSO (-) for the indicated time (h = hour). Total cell lysates (30 μg) were blotted as indicated. Note that EGFP-Nrf2 migrates as doublet of approximately 130 kDa. Data are representative of three independent experiments. (C,D) CK-666 induces nuclear translocation of Nrf2. EGFP-Nrf2-expressing cells were plated on collage I-coated coverslips, treated with CK-666 (100 μM) or DMSO (-) for the indicated time (min = minutes) and scored only if the nuclear *vs.* cytosolic intensity ratio of EGFP-Nrf2 (nuclear/cytosolic Nrf2 intensity > 1) was bigger than one. Bar graph depicts percentage of scored cells (mean and SEM) (* = $p < 0.05$; ** = $p < 0.01$; One-way ANOVA with Bonferroni's correction for multiple comparisons, n = 3). Representative compressed confocal Z-stacks of the cells analysed in C are depicted in D. Bar is 20 μm. Parallel experiments showed that CK-666 reduced lamellipodium formation and phallodin staining (not shown and Fig. S6). (E,F) Latrunculin A, but not SMIFH2, mimics the effects of CK-666. Representative compressed confocal Z-stacks of the cells analysed in E are depicted in F. Bar is 10 μm. Parallel experiments showed that Latrunculin A disrupted the actin cytoskeleton, whereas SMIFH2 reduced stress fibre-like actin structures (not shown and Fig. S6). (G) EGFP-Nrf2 partially colocalizes with F-actin. Representative confocal central sections depicting EGFP-Nrf2-expressing keratinocytes. Nuclei (DAPI, blue in merge), actin cytoskeleton (Phalloidin, red in merge) and EGFP-Nrf2 (EGFP-Nrf2, green in merge) are shown. Bar is 20 μm. Position of insets (i and ii, bar is 5 μm) is marked by white squares.

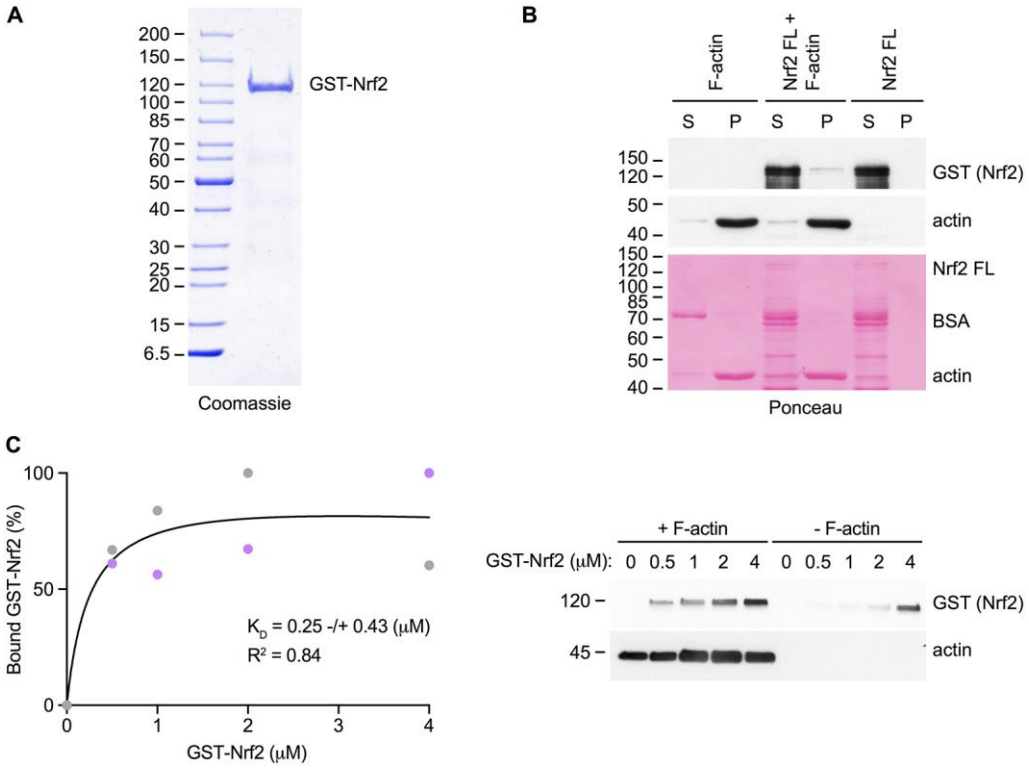

Fig. 8. Nrf2 binds directly to filamentous actin.

(A) Coomassie gel showing purified recombinant full-length GST-Nrf2 (4 μg). (B) Co-sedimentation assays were performed mixing GST-Nrf2 (Nrf2 FL, 0.15 μM with Bovine Serum Albumin (BSA, 0.6 μM) and either F-actin (F-actin, 2.5 μM) or F-actin buffer. The same percentages of soluble (S) and pelleted (P) fractions were subjected to SDS-PAGE followed by immunoblotting as indicated. Ponceau serves as a loading control. Data are representative of three independent experiments performed using three different actin and Nrf2 batches. (C) The affinity of interaction between Nrf2 and F-actin is 0.25 μM. Full-length GST-Nrf2 (0, 0.5, 1, 2 and 4 μM) was sedimented with (+ F-actin, 2.5 μM) or without F-actin (- F-actin). The same percentage of each pelleted fraction was immunoblotted as indicated. Band intensities were measured with QuantityOne. Specific Nrf2 bound fractions (Bound GST-Nrf2 (%)) were obtained subtracting the intensity of Nrf2 without F-actin to the intensity of Nrf2 with F-actin, followed by normalization. Grey and lilac dots corresponding to two independent experiments were used for the fitting (shown as a black line). The computed equilibrium dissociation constant (K_D) is expressed as mean and SD. R^2 indicated that coefficient of determination of the fitting.

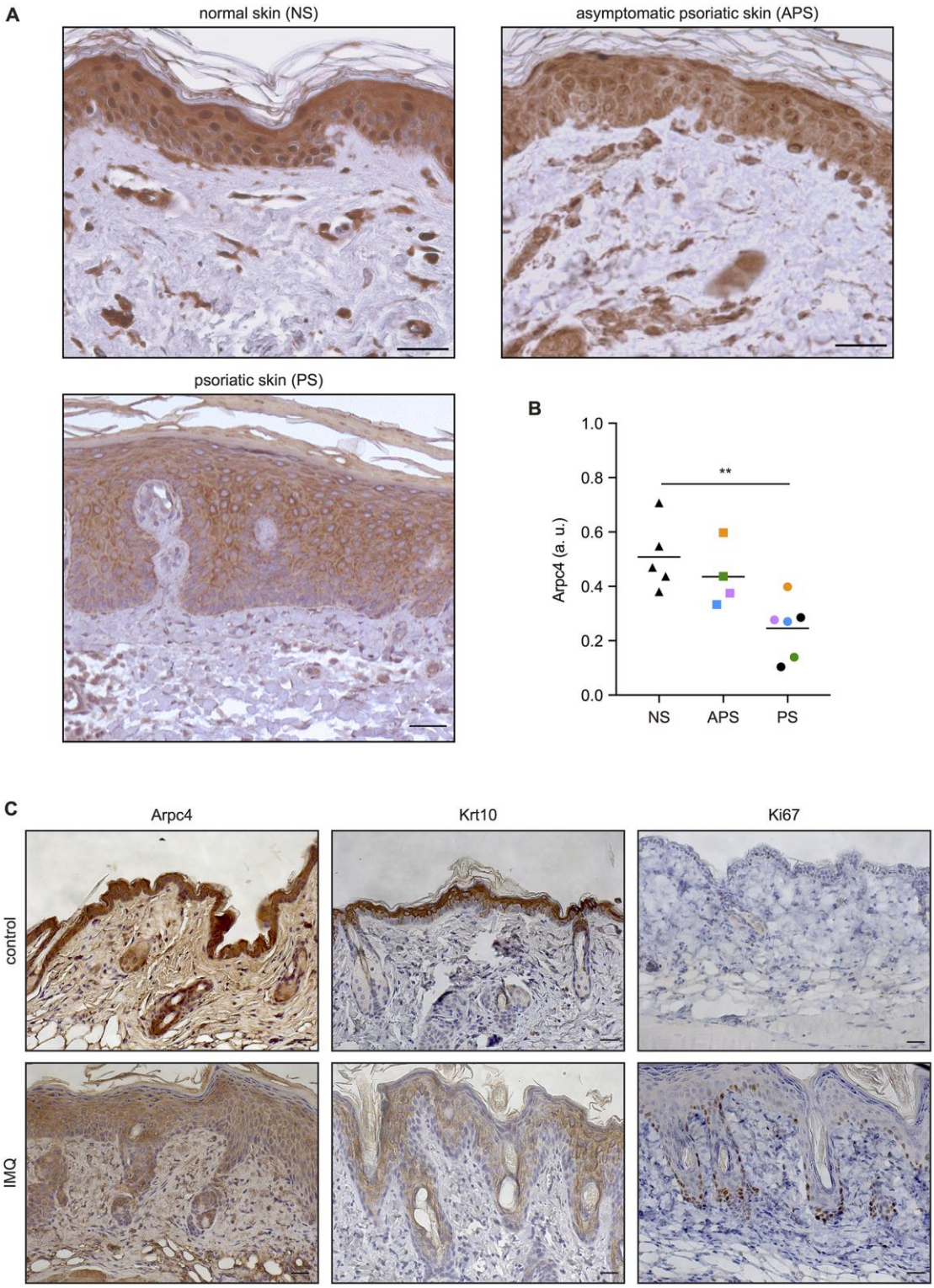

Fig. 9. Human and mouse psoriatic skin show reduced Arpc4 expression.

(A) Arpc4 is downregulated in human psoriatic skin. Representative images showing anti-Arpc4 immunoreactivity (brown staining) in normal skin (NS), asymptomatic psoriatic skin (APS) and psoriatic skin (PS) sections. Samples were processed, stained and acquired in parallel. Note that APS and PS are from the same patient. Bars, 500

μm. (B) Arpc4 levels are significantly reduced in the epidermis of psoriatic patients. Arpc4 immunoreactivity in the NS, APS and PS samples images shown in Fig. S7 was quantified, normalized and plotted as arbitrary units (a. u.) so that back and white would correspond to one and zero, respectively. Graph depicts means (black bars) and individual Arpc4 values colour-coded according to frame colour of the corresponding images. Identical colours denote matched APS and PS samples (** = $p < 0.01$; One-way ANOVA with Bonferroni's correction for multiple comparisons). (C) Arpc4 is downregulated in IMQ-treated mouse epidermis. Skin sections of control and IMQ-treated B6 mice were stained with anti-Arpc4, anti-Krt10, and anti-Ki67 antibodies. Samples were processed, stained and acquired in parallel. Representative images are shown. Bar is 50 μm.

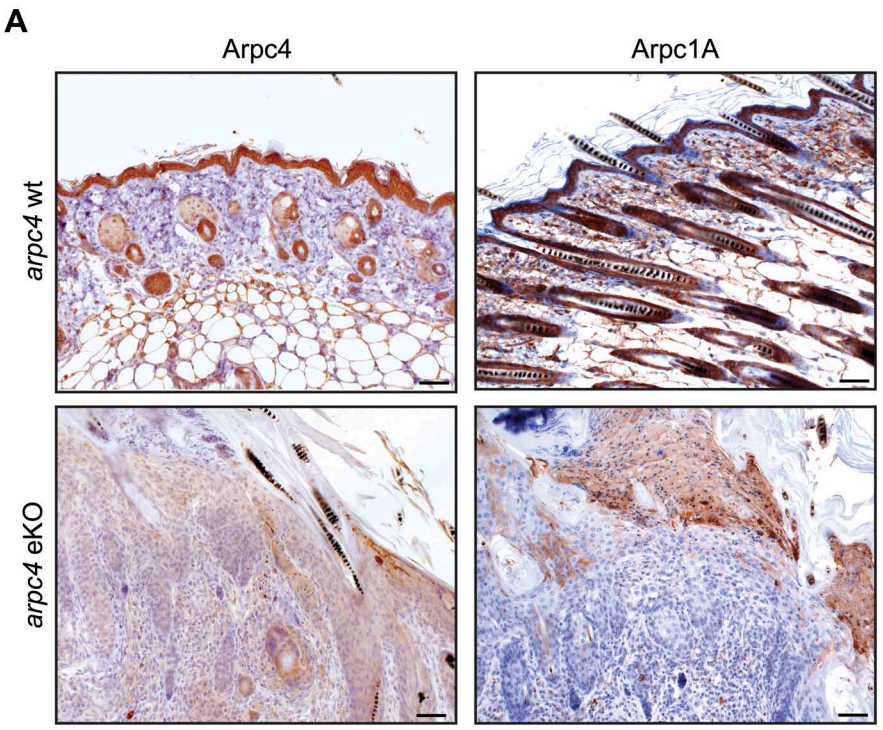

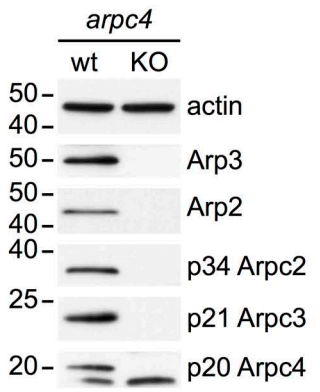

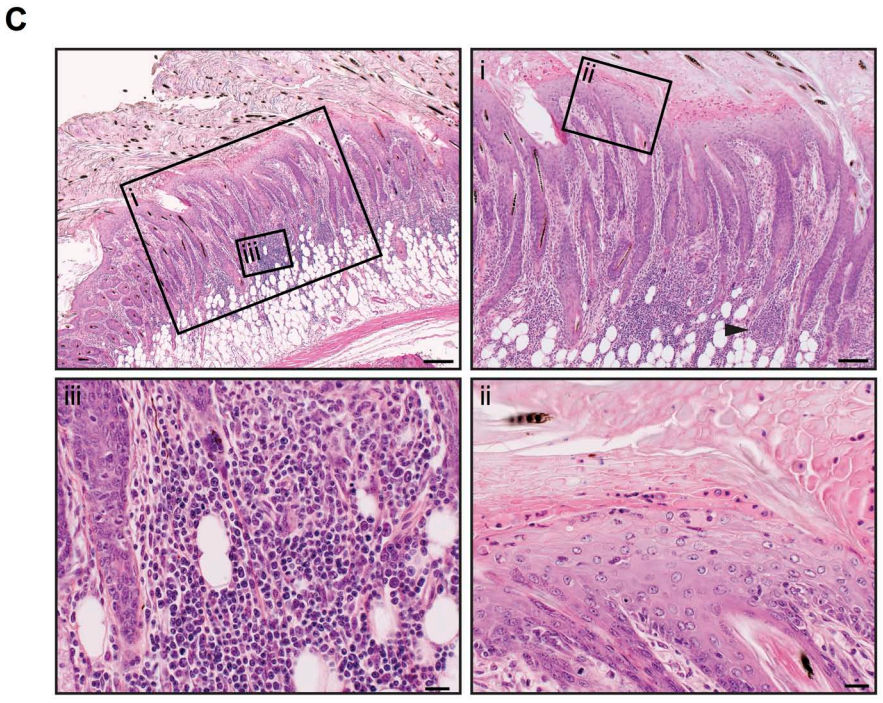

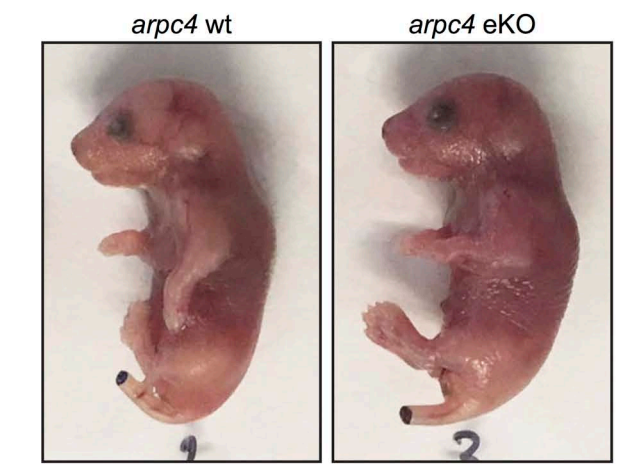

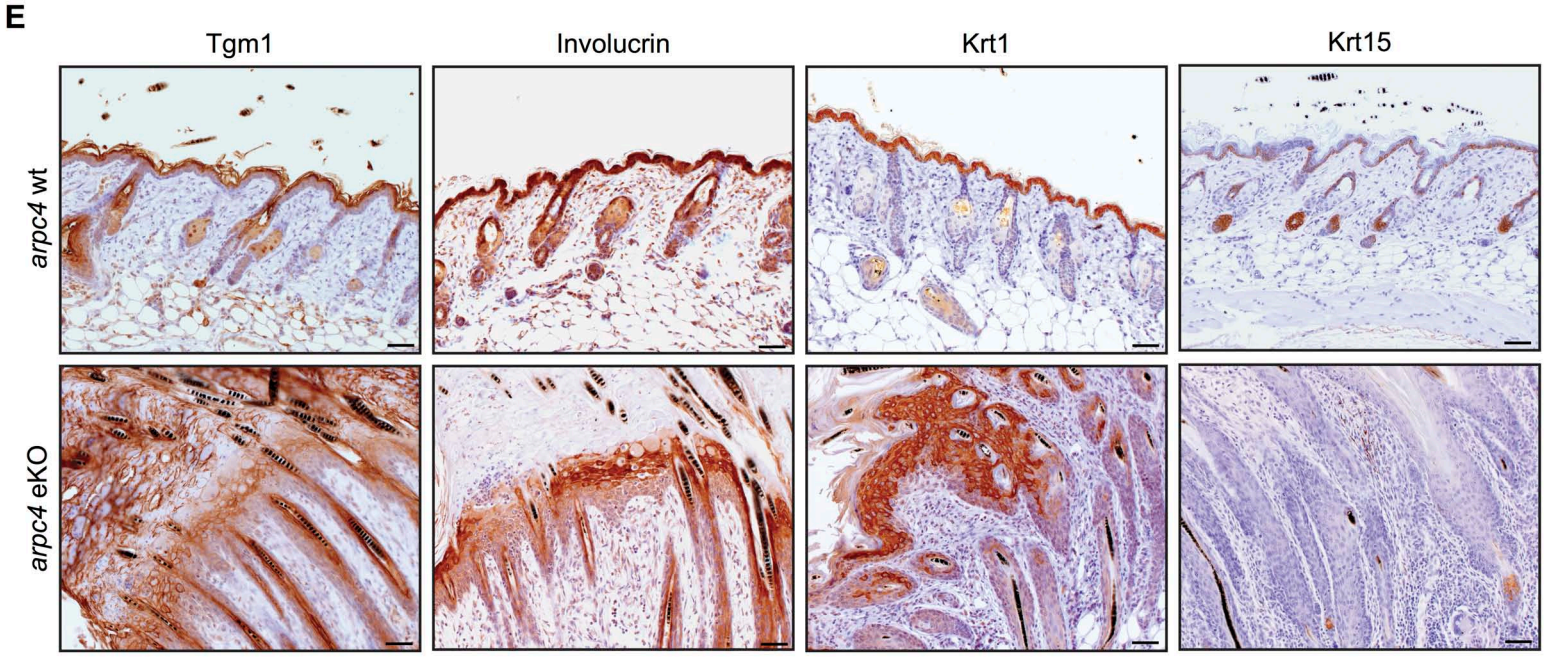

van der Kammen et al., Figure S1

Fig. S1. Additional characterization of the *arpc4* eKO mice.

(A) Immunohistochemical characterization of the skin of *arpc4* wt and *arpc4* eKO littermates at day 14 after birth. Skin was isolated, fixed, cut and stained with anti-Arpc4 and anti-Arpc1A antibodies. Representative images of normal skin (*arpc4* wt) and psoriasis-like lesions (*arpc4* eKO) are shown. Bar is 50 μm. (B) Characterization of *arpc4*$^{f/f}$ (*arpc4* wt) and *arpc4*$^{f/f}$*::K14*-Cre(neo) (*arpc4* KO) keratinocytes. Total cell lysates (30 μg) were blotted as indicated and actin was used as a loading control. The lower band in the p20 Arpc4 blot is a non-specific cross-reacting protein species. (C) The *arpc4* eKO mice show a psoriasis-like phenotype. A representative psoriasis-like lesion found in the skin of the *arpc4* eKO mice at day 21 after birth is shown. Bar is 200 μm. Inset i zooms in to structures resembling psoriatic rete ridges (Bar is 100 μm). Inset ii and iii depict ghost cells and inflammatory infiltrates, respectively. Arrowhead marks a microabscess. (D) The *arpc4* eKO pups do not exhibit any outside-in epidermal permeability barrier defects. Newborn mice were euthanized and, after clipping the tail tip, subjected to skin permeability assays. Pictures show representative wild-type (*arpc4* wt) and knockout (*arpc4* eKO) pups taken from one of two littermates giving identical results. Dye penetration from the wounded tail served as a positive internal control. (E) Immunohistochemical analysis of the skin of *arpc4* wt and *arpc4* eKO mice. Skin was isolated, fixed, cut and stained with the indicated antibodies. Representative skin sections of *arpc4* wt and *arpc4* eKO mice at day 21 after birth are shown. Bar is 50 μm.

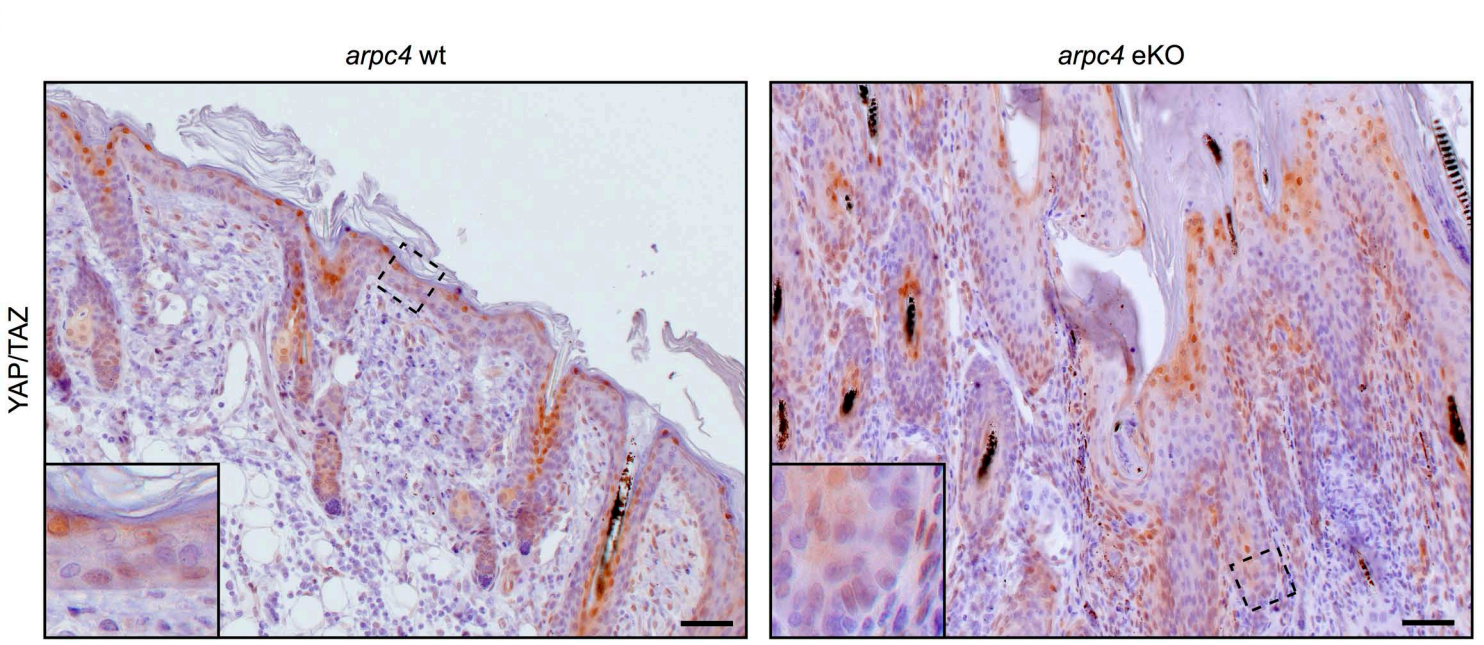

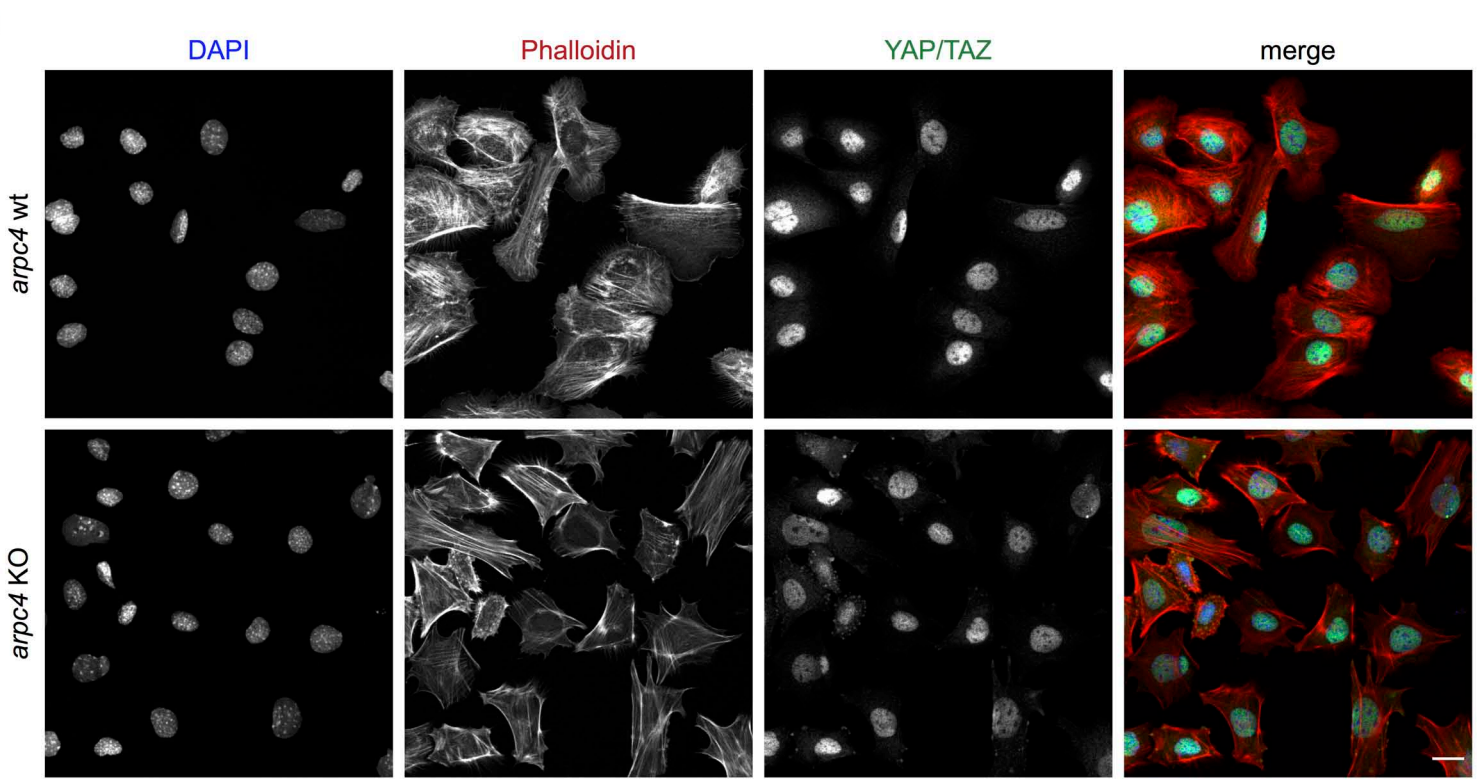

van der Kammen et al., Figure S2

Fig. S2. Keratinocytes lacking the Arp2/3 complex show unperturbed expression and localization of YAP/TAZ both in tissue culture and *in vivo*.

(A) YAP/TAZ expression and localization are not perturbed in the epidermis of *arpc4* wt and *arpc4* eKO mice. Skin was isolated, fixed, cut and stained with anti-YAP/TAZ antibodies. Representative skin sections of *arpc4* wt and *arpc4* eKO mice at day 21 after birth are shown. Bar is 50 μm. (B) YAP/TAZ expression and localization are not perturbed in *arpc4* wt and *arpc4* eKO keratinocytes. Immortalized wild-type (*arpc4* wt) and knockout (*arpc4* KO) keratinocytes derived from those characterized in Fig. S1B were plated on collagen I-coated coverslips. Coverslips were fixed and processed in parallel, and confocal Z-stacks acquired using identical settings. Representative compressed confocal Z-stacks show YAP/TAZ (green in merge) the actin cytoskeleton (Phalloidin, red in merge) and nuclei (DAPI, blue in merge). Bar is 20 μm. Data are representative of two independent experiments.

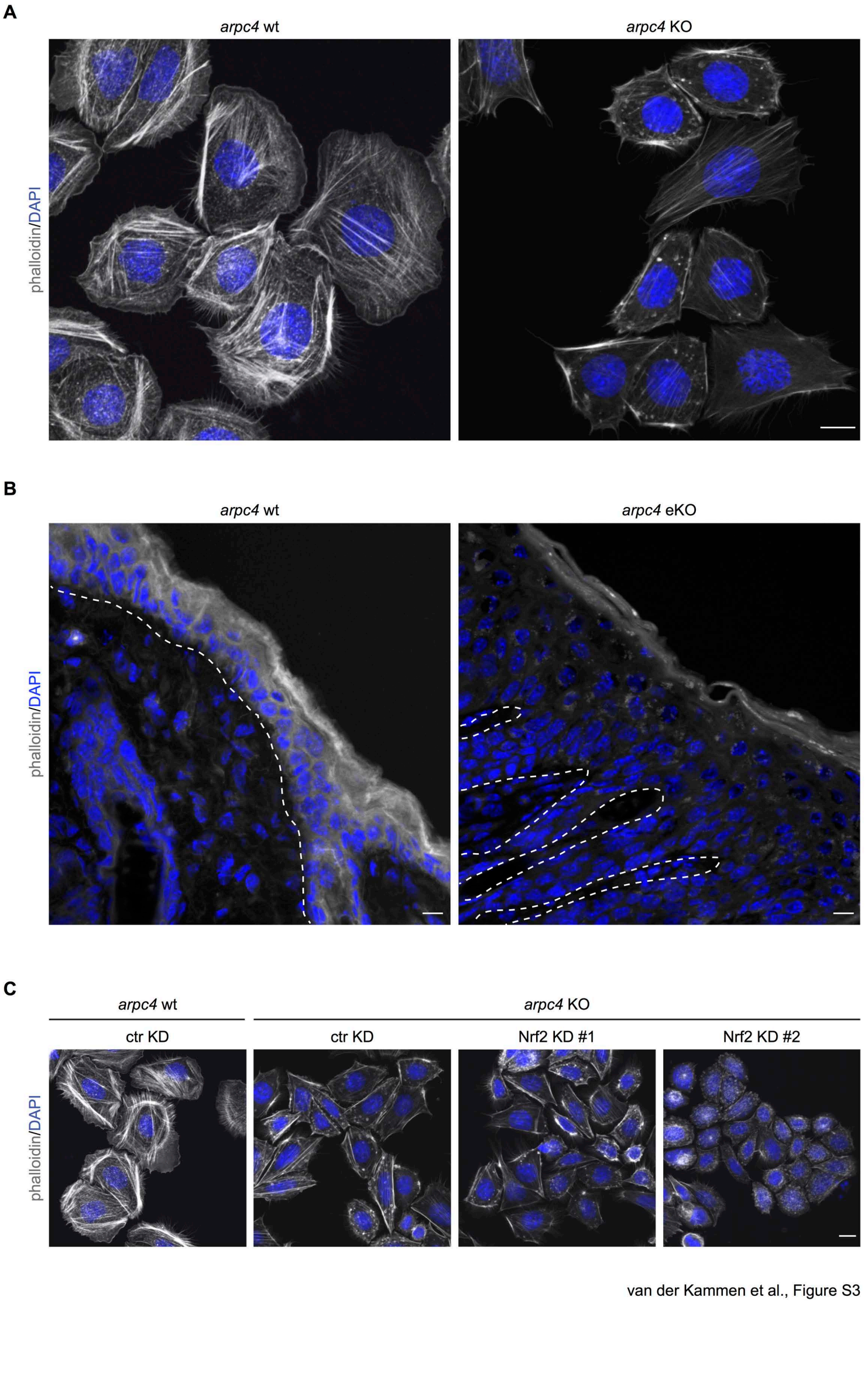

van der Kammen et al., Figure S3

Fig. S3. Keratinocytes lacking the Arp2/3 complex have a perturbed actin cytoskeleton both in tissue culture and *in vivo*.

(A) The *arpc4* knockout keratinocytes are smaller and do not form either lamellipodia or ruffles. Wild-type (*arpc4* wt) and knockout (*arpc4* KO) keratinocytes characterized in Fig. 4A were plated on collagen I-coated coverslips. Coverslips were always fixed and processed in parallel, and confocal Z-stacks acquired using identical settings. Representative compressed confocal Z-stacks show the actin cytoskeleton (Phalloidin, grey in merge) and nuclei (DAPI, blue in merge). Bar is 10 μm. Data are representative of three independent experiments. (B) F-actin is reduced in the epidermis of the *arpc4* eKO mice. Four-micrometer thick cryo-sections of the epidermis of *arpc4* wt and *arpc4* eKO mice at day 9 after birth were fixed with PFA for 10 minutes, blocked in PBS-BSA 5% for 30 minutes and subsequently stained with TRITC-phalloidin (grey in merge) and DAPI (blue in merge) to detect F-actin and nuclei, respectively. Confocal images were acquired using a 40 x objective and identical settings. Representative compressed confocal Z-stacks sections are shown. Dashed white lines demark the epidermal boundaries. Bar is 10 μm. (C) Downregulation of Nrf2 in the *arpc4* KO keratinocytes does not affect the actin cytoskeleton. The cells characterized in Fig. 4D were plated on collagen I-coated coverslips. Coverslips were always fixed and processed in parallel, and confocal Z-stacks acquired using identical settings. Representative compressed confocal Z-stacks show the actin cytoskeleton (Phalloidin, grey in merge) and nuclei (DAPI, blue in merge). Bar is 10 μm. Data are representative of two independent experiments.

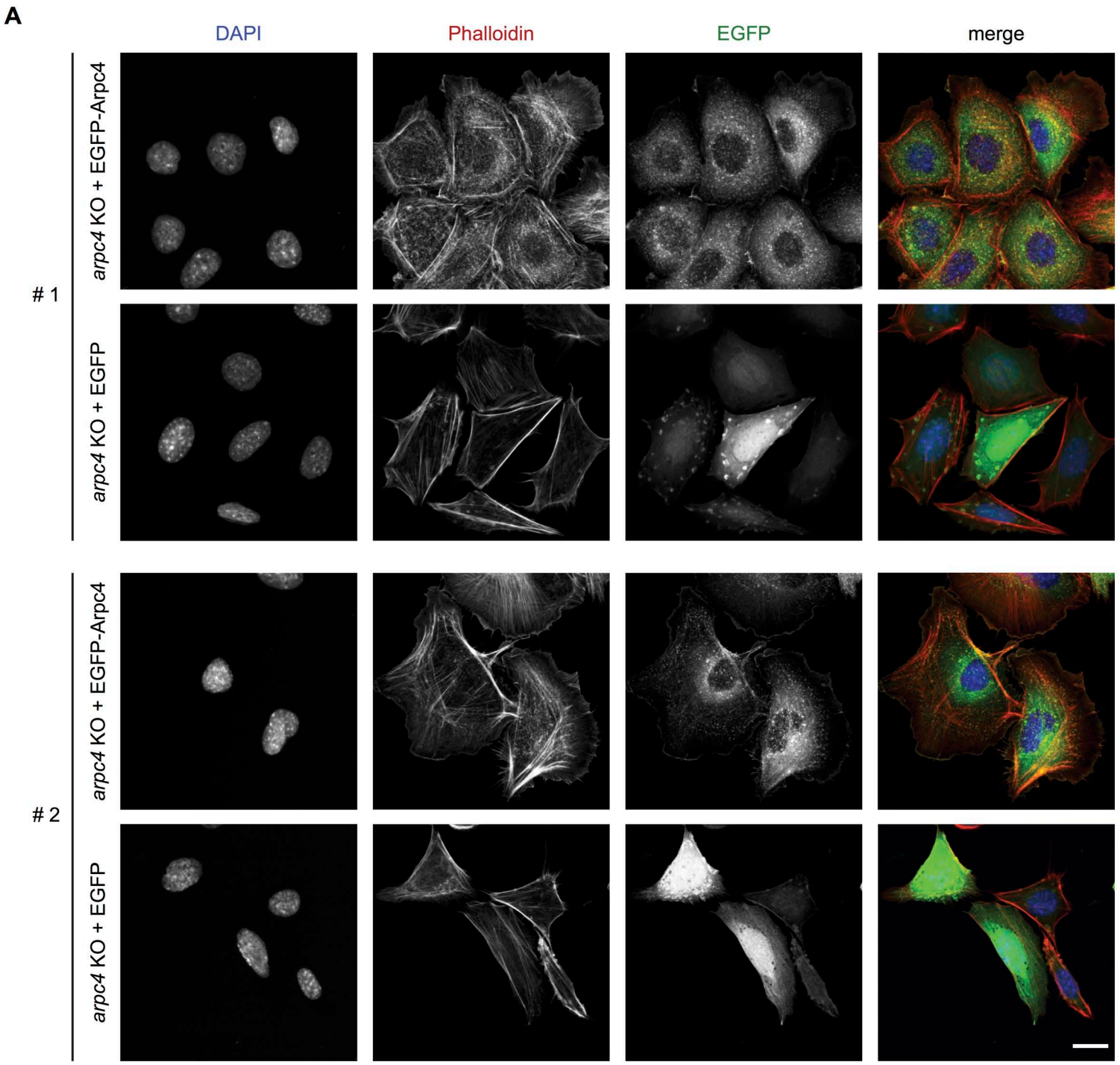

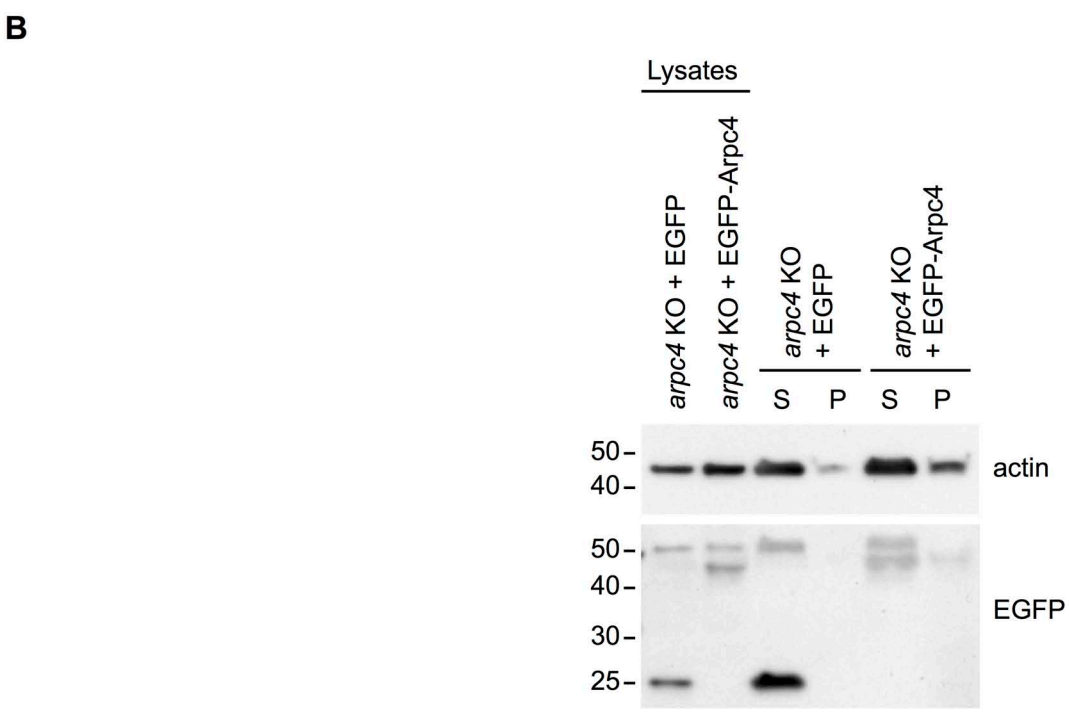

van der Kammen et al., Figure S4

Fig. S4. Characterization of a second line of isogenic Arp2/3 complex knockout and rescued keratinocytes.

(A) Morphological characterization of the isogenic Arp2/3 complex knockout and rescued keratinocytes. Two independent isogenic Arp2/3 complex knockout (*arpc4* KO + EGFP) and rescued keratinocytes (*arpc4* KO + EGFP-Arpc4) (line #1 = #1; line #2 = #2, see also Fig. 5A) were plated on collagen I-coated coverslips. Coverslips were fixed and processed in parallel, and confocal Z-stacks acquired using identical settings. Representative compressed confocal Z-stacks show nuclei (DAPI, blue in merge), actin cytoskeleton (Phalloidin, red in merge) and either EGFP or EGFP-Arpc4 (EGFP, green in merge). Bar is 20 μm. Data are representative of three independent experiments. (B) Distribution of G-actin and F-actin in the isogenic Arp2/3 complex knockout and rescued keratinocytes. *arpc4* KO + EGFP and *arpc4* KO + EGFP-Arpc4 keratinocytes (line #2) were plated on collagen I-coated dishes, harvested, lysed for separating the G-actin and F-actin pools. Total cell lysates (30 μg) and the same percentage of both the soluble (S) and the pelleted (P) material were blotted as indicated. Cross-reacting bands of about 50 kDa are visible in the anti-EGFP blot.

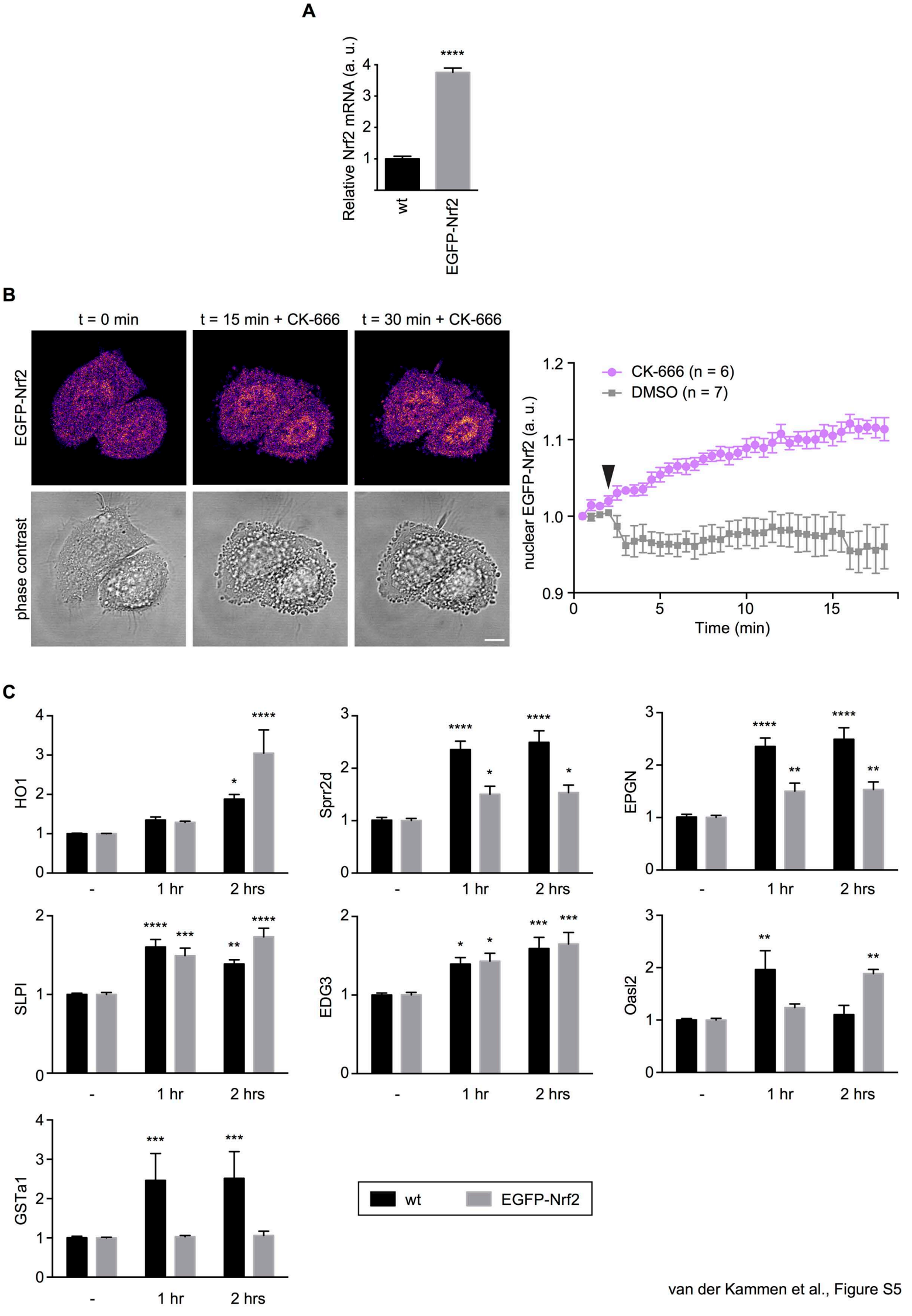

van der Kammen et al., Figure S5

Fig. S5. Additional characterization of the EGFP-Nrf2-expressing keratinocytes and response thereof to CK-666.

(A) Characterization of the EGFP-Nrf2-expressing keratinocytes. The relative levels of the Nrf2 messenger RNA (mRNA) (a. u. = arbitrary units) in wild-type (wt) and EGFP-Nrf2-expressing keratinocytes shown in Fig. 7B were determined by RT-qPCR. Data are expressed as mean and SEM (n = 6 from two independent experiments; **** = $p < 0.0001$, unpaired two-tail t test). (B) CK-666 induces nuclear translocation of Nrf2. EGFP-Nrf2-expressing keratinocytes were plated on collagen I-coated glass-bottom dishes, imaged prior and after the addition of CK-666 (100 μM). *Left.* Selected frames extracted from Movie S2 are shown. Bar is 10 μm. *Right.* Integrated intensities of nuclear EGFP-Nrf2 were determined using ImageJ and initial values used as a reference for normalization. Bar graph depicts mean and SEM of normalized nuclear EGFP-Nrf2 (a. u. = arbitrary units) over time (min = minutes) as obtained from CK-666- and DMSO-treated cells (n = number of cells pooled from two independent experiments). Black arrowhead indicates addition of either CK-666 (lilac curve) or DMSO (grey curve). The minor reduction in intensity recorded in the DMSO-treated cells may be due to a change in auto-fluorescence caused by the added medium and/or the DMSO itself, or photobleaching. (C) CK-666 increases the expression of Nrf2-target genes. Wild-type (wt) and EGFP-Nrf2-expressing keratinocytes (EGFP-Nrf2) were treated with either DMSO (-) or CK-666 (100 μM) for the indicated time (1 h = 1 hour; 2 h = 2 hours). Total RNA was used to compare the relative expression of the indicated genes (on the Y axis) by RT-qPCR. Data are expressed as mean and SEM ($n \geq 6$ from at least two independent experiments; * = $p < 0.05$; ** = $p < 0.01$; *** = $p < 0.001$; **** = $p < 0.0001$, One-way ANOVA with Bonferroni's correction for multiple comparisons). The delay between nuclear accumulation of Nrf2 and upregulation of its target genes is likely due to the different sensitivity of the image-based and RT-qPCR analyses. Moreover, a unique combination of transcriptional activators and repressors binding to the promoter of each analyzed gene determines steady-state transcript levels, as well as magnitude and kinetics of the response to CK-666.

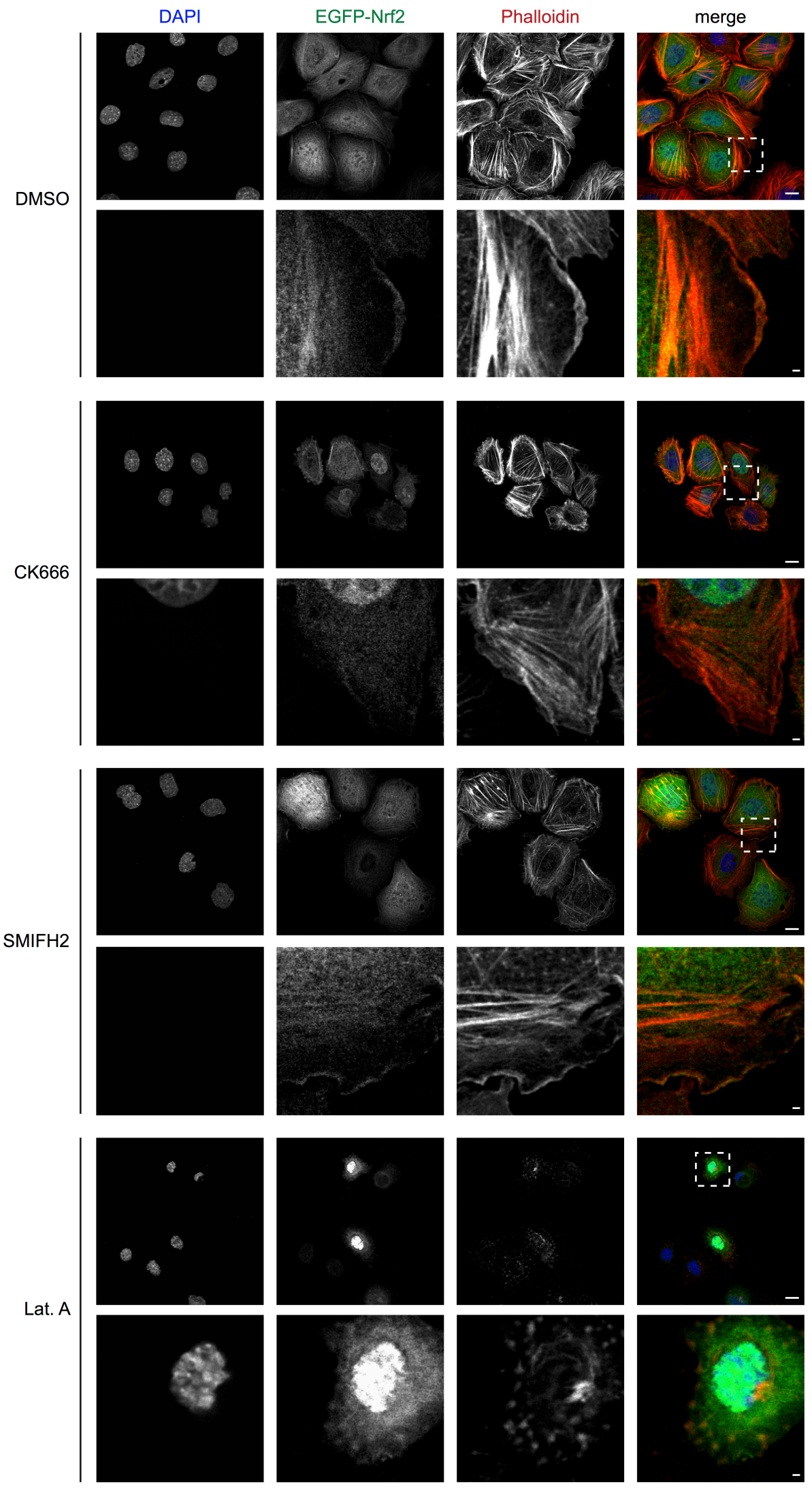

van der Kammen et al., Figure S6

Fig. S6. The association of EGFP-Nrf2 with F-actin is perturbed by CK-666 and Latrunculin A, but not SMIFH2.

EGFP-Nrf2-expressing keratinocytes were treated with either DMSO, or CK-666 (100 μM), or SMIFH2 (3 μM), or Latrunculin A (Lat. A, 0,25 μM). Representative compressed confocal Z-stacks show nuclei (DAPI, blue in merge), EGFP-Nrf2 (EGFP-Nrf2, green in merge) and actin cytoskeleton (Phalloidin, red in merge). Bars are 20 μm. Dashed white squares mark the position of the insets shown below each image (bars are 2 μm).

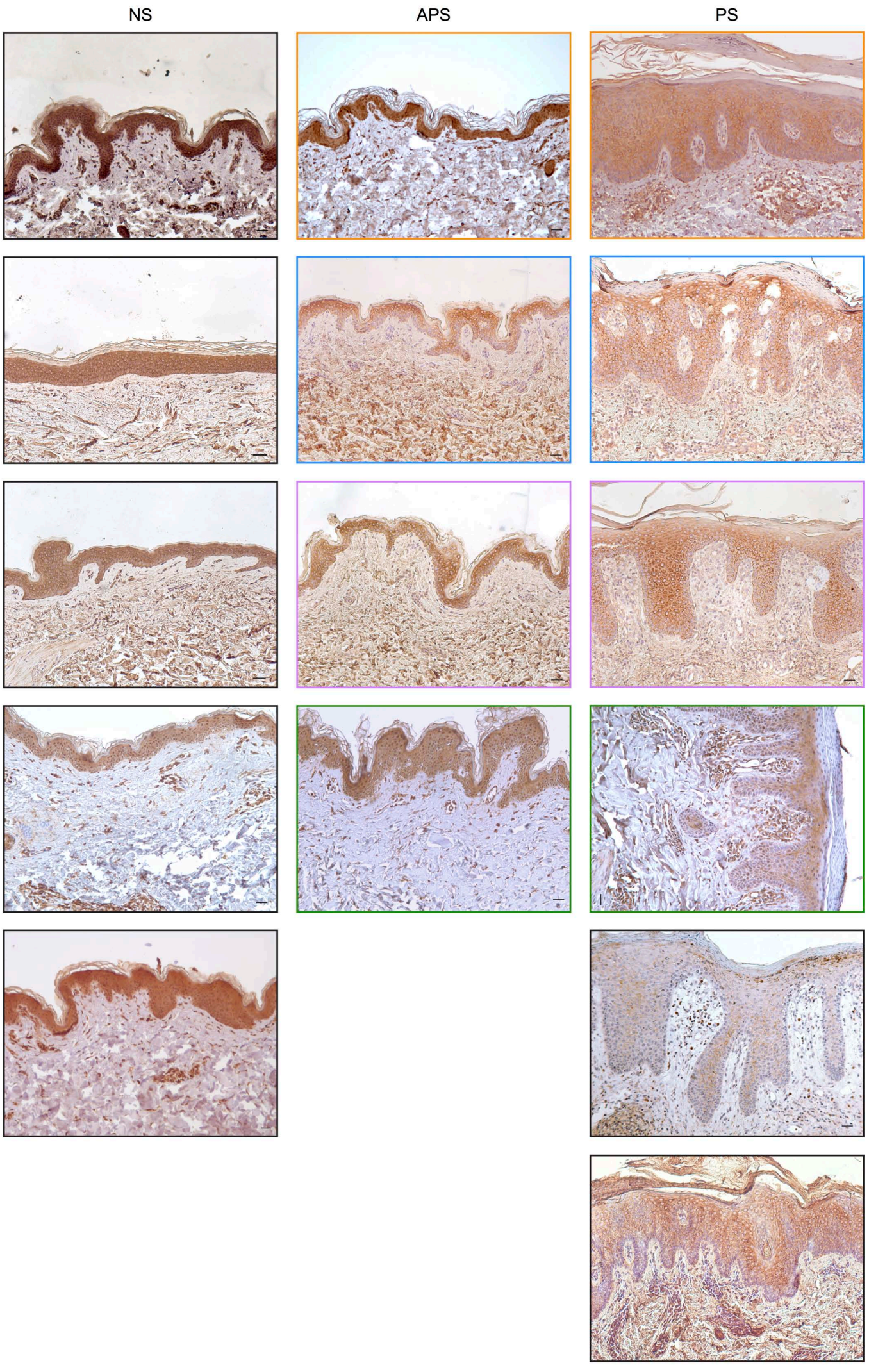

van der Kammen et al., Figure S7

Fig. S7. Gallery of human skin samples stained with anti-Arpc4 antibodies.

Gallery of the images quantified in Fig. 9B. Normal skin (NS) sections, asymptomatic psoriatic skin (APS) and psoriatic skin (PS) sections were stained with anti-Arpc4 antibodies (brown staining). Asymptomatic psoriatic skin and psoriatic skin sections obtained from the same patient have identical frame colours, which match dot colours in Fig. 9B. Bars, 200 μm.

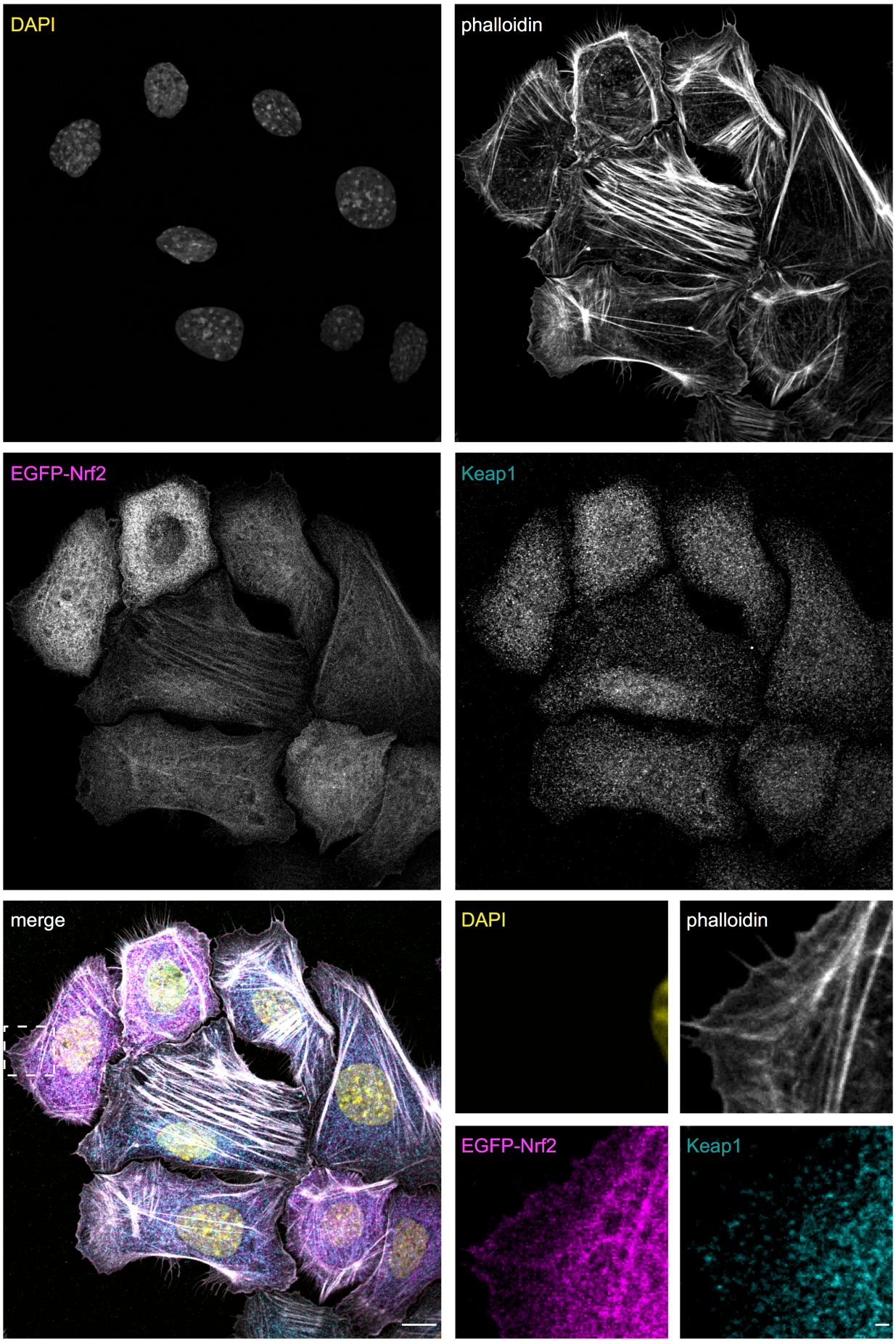

van der Kammen et al., Figure S8

Fig. S8. Endogenous Keap1 is diffused and uniformly distributed in keratinocytes.

Representative confocal basal section of EGFP-Nrf2-expressing keratinocytes. Nuclei (DAPI, yellow in merge), actin cytoskeleton (Phalloidin, grey in merge), EGFP-Nrf2 (EGFP-Nrf2, magenta in merge) and Keap1 (cyan in merge) are shown. Bar is 20 μm. Position of the inset is marked by white dashed square (bar is 2 μm).

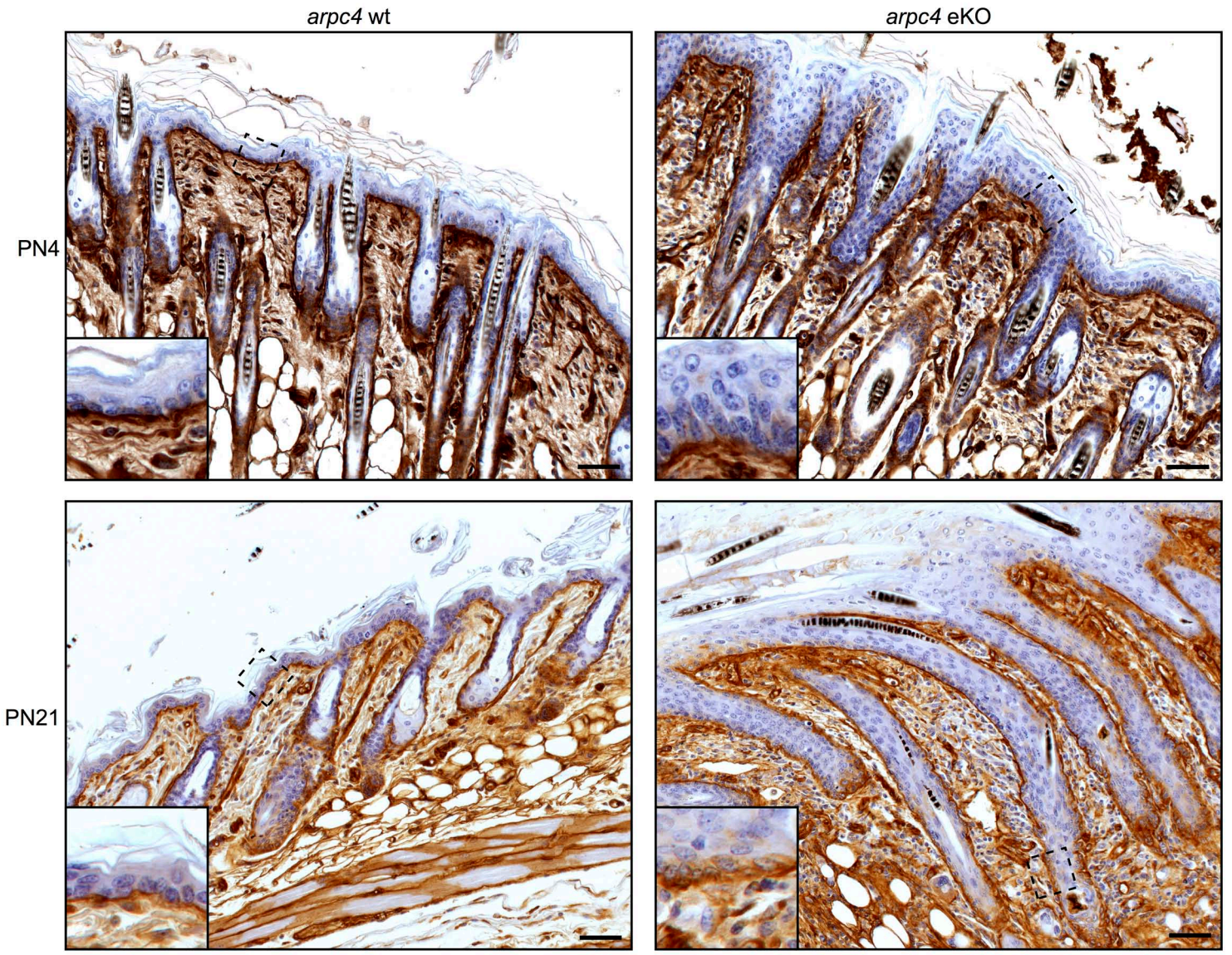

van der Kammen et al., Figure S9

Fig. S9. Basement membrane is only mildly disturbed in young *arpc4* eKO pups. Skin of *arpc4* wt and *arpc4* eKO littermates was fixed, processed and stained in parallel at either PN4 or PN21. Images depict representative skin sections stained with anti-Laminin antibodies to highlight the basement membrane and dashed boxes mark zoomed-in regions. Note the slightly jagged and unevenly distribution of Laminin in the psoriasis-like lesions at PN21. Bar is 50 μm.

Supplementary Movies

Movie S1. *arpc4* wt and *arpc4* eKO littermates.

Time lapse showing *arpc4* wt and *arpc4* eKO littermates at day 7 after birth.

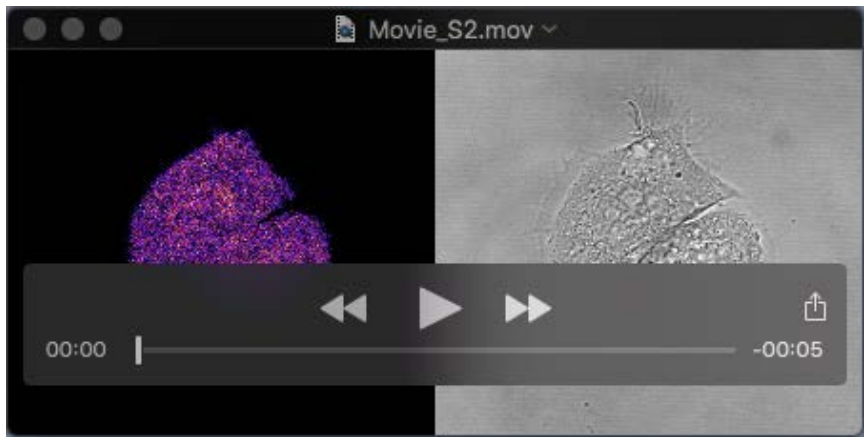

Movie S2. Confocal time-lapse video microscopy showing the effects of CK-666 on EGFP-Nrf2-expressing keratinocytes.

CK-666 induces nuclear accumulation of Nrf2. EGFP-Nrf2-expressing keratinocytes were plated on collagen I-coated glass-bottom dishes, imaged prior to and after the addition of CK-666 (100 μM).

Supplementary Tables

Table S1. Differentially expressed genes in wild-type *vs.* KO epidermises.
Inventory of the 141 differentially expressed genes along with reads, computed *p* values and Log_2 fold changes. Nrf2-responsive genes are highlighted in light blue.

Click here to Download Table S1

Table S2. Ingenuity Pathway Analysis (IPA) of differentially expressed epidermal genes.
Sheet 1: Legend
Sheet 2: Full Ingenuity Pathway Analysis (IPA) of the "Diseases and Disorders" associating with the differentially expressed genes having IPA annotation (134 of 141).
Sheet 3: Full Ingenuity Pathway Analysis report of the diseases and biofunctions associated with the category "Dermatological Diseases and Conditions".

Click here to Download Table S2

Table S3. Differentially expressed genes in wild-type *vs.* KO keratinocyte.
Inventory of the 109 differentially expressed genes along with reads, computed *p* values and Log_2 fold changes.

Click here to Download Table S3

Table S4. List of the primary antibodies employed in this study.
Names, origin and working conditions are indicated.

Click here to Download Table S4

Table S5. List of the RT-qPCR primers employed in this study.
Gene names, accession numbers and primer sequences are indicated.

Click here to Download Table S5